RSC Advances

PAPER

View Article Online
View Journal | View Issue

Cite this: *RSC Adv.*, 2026, **16**, 23257

Design, synthesis, and anti-inflammatory evaluation of new isatin azo disperse dyes: computational studies, molecular docking, and printing performance on polyester fabrics

Hend A. Hekal, *[a] Elkhabiry Shaban,*[b] Zeinab A. Elshahid,[c] Hayam A. Abd El Salam,[d] Faten M. Atlam[e] and Ahmed A. Nosier[af]

Pharmaceutical and industrial uses of heterocyclic compounds are so varied that they are important for material science and drug discovery. First synthesized in 1841, isatin is a derivative of indole that has garnered significant attention as a structure that is modular for bioactive chemicals. In this study, novel isatin-based azo dyes, namely 2-cyano-*N*′-(4-hydroxy-3-methoxy)-(*E*)-(aryl)diazinyl)benzylidene)-2-((*Z*)-2-oxoindolin-3-ylidene) acetohydrazides (**4a–d**) and (*E*)-5-(2-cyano-2-((*Z*)-2-oxoindolin-3-ylidene)acetyl)-3-(3,5-dimethoxyphenyl)-1-(aryl)formazans (**5a–d**), were effectively synthesized and their structure was clarified using spectroscopic investigations utilizing mass spectrometry, ^{1}H, ^{13}C NMR, and FT-IR. The colorimetric and fastness characteristics of the dyes, such as their resistance to light, perspiration, washing, sublimation, and rubbing, were assessed after they were applied to printing polyester fabric. An assessment of the anti-inflammatory properties of synthetic isatin azo dyes revealed that almost all of them exhibit anti-inflammatory actions against COX-2, TNF, and IL-6. Additionally, using the 6-311++G(d, p) basis set, density functional theory (DFT) was used to study the isatin azodyes **4a–d** and **5a–d**. The energy values of the highest filled molecular orbital (HOMO), the lowest unfilled molecular orbital (LUMO), and the MEP were measured to discover more about the reactive regions of the molecules. To illustrate the connection between theory and experiment, FT-IR spectra were calculated for isatin dye molecules. Excellent agreement was established between experimental and theoretical data. In conclusion, every newly created dye has the potential to be an anti-inflammatory. Compounds **4b** and **5b** were shown to be the most efficient against TNF and IL-6, and theoretical evidence supports these findings. To gain more insights into how compound **5b** interacts with TNF (tumor necrosis factor), we used molecular docking tools to predict its affinity within the receptor, providing useful preliminary evidence for drug development. Additionally, docking analysis was performed, and it confirmed the presented results.

Received 16th February 2026
Accepted 20th April 2026

DOI: 10.1039/d6ra01392a

rsc.li/rsc-advances

Introduction

One of the most significant classes of chromophores, azo dyes, has many applications in the scientific, industrial, and medical domains. Researchers have studied simple synthesis techniques for azo dyes and their derivatives, which have a variety of potential applications. The basic skeletal structure of azo chromophores, a type of chemical molecule that is a colorant, contains azo groups.[1,2] The nitrogen–nitrogen double bond (–N=N–), which distinguishes azo dyes, offers the textile industry various advantages. In this sense, heterocyclic compounds that contain sulfur, nitrogen, or oxygen are essential for azo dyes to produce a variety of hues and increase the dye's color. Azo dyes with heterocyclic moieties now outperform those made from simple aromatic amines in terms of coloring characteristics, potency strength, thermal capacity, and more favorable solvatochromic behavior.[3,4] Additionally, the procedure of applying color to fabric with patterns or designs is known as textile printing, as opposed to dyeing.[5,6] Therefore, various factors, such as the kind and amount of dyes selected, might affect the dyes utilized for printing.[6] Other factors that

[a]*Organic Chemistry, Chemistry Department, Faculty of Science, Tanta University, Tanta, 31527, Egypt. E-mail: hend.hekal@science.tanta.edu.eg; ahmed.nosir@science.tanta.edu.eg*

[b]*Dyeing, Printing and Textile Auxiliaries Department, Textile Research and Technology Institute, National Research Centre, Dokki, Giza 12622, Egypt. E-mail: shaban_nrc@yahoo.com*

[c]*Chemistry of Natural and Microbial Products Department, Pharmaceutical Industry and Research Institute, National Research Centre, Giza, 12622, Egypt. E-mail: dr.z.a.elshahid@gmail.com*

[d]*Green Chemistry Department, National Research Centre, Dokki, Giza 12622, Egypt. E-mail: yooma_nrc82@yahoo.com*

[e]*Theoretical Applied Chemistry Unit (TACU), Chemistry Department, Faculty of Science, Tanta University, Tanta, 31527, Egypt. E-mail: faten.atlam@science.tanta.edu.eg*

[f]*Alamal College for Specialized Medical Sciences, Karbala, 56001, Iraq*

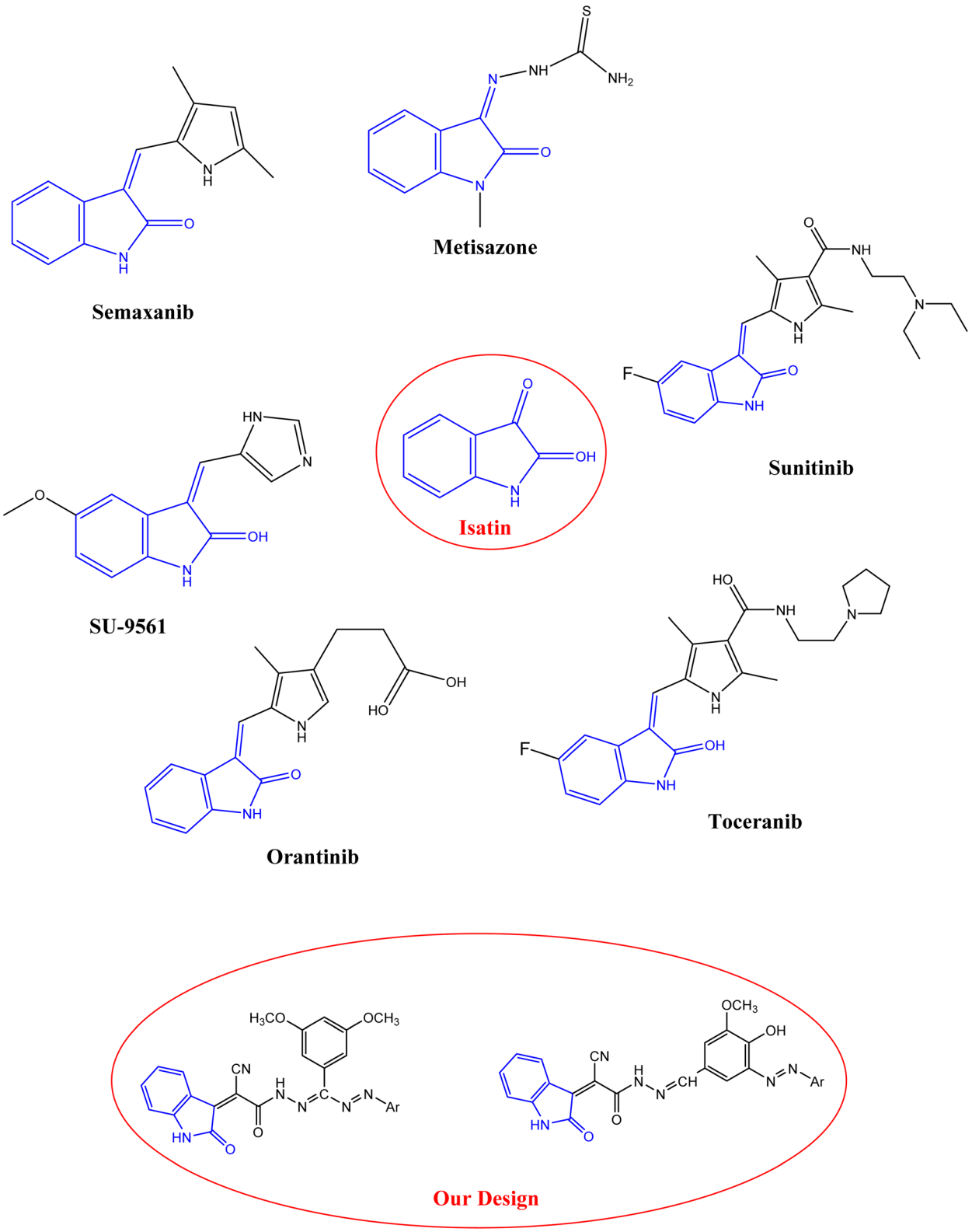

Fig. 1 Some examples of marketed isatin derivative candidates.

affect such dyes include the type of thickening chosen, the composition of the thick and sticky printing paste, the fiber composition, and the design of the fabric to be printed. Azo dyes are well-known colored substances that are widely used in a variety of textile materials (such as leather and fiber) as well as the printing, paint, and cosmetics industries.[5] Previous studies have shown that the heterocyclic ring's azo chromophore boosts the compound's possible pharmacological action. Isatin (I, 1*H*-

indole-2,3-dione; Fig. 1) is a heterocyclic compound that was first created about 170 years ago.[7,8] Isatin's many chemically reactive functional groups make it more valuable for synthesis purposes. Because of this, it is regarded as a preferred substrate in organic and medicinal chemistry, where it is frequently used to produce a variety of bioactive compounds with a wide spectrum of biological actions, including anticancer,[9] anti-HIV,[10] antiviral,[11] antitumor,[12] antifungal,[13] antimalarial,[14] antioxidant,[15] anti-inflammatory,[16] antimicrobial,[17] analgesic,[18] anticonvulsants,[19] and so on. Numerous conventional isatin analogs are already used in medicine, and Fig. 1 lists a few commercially available drugs that exploit isatin scaffolding to treat a range of ailments. Azo dyes' physicochemical and dyeing qualities are improved by adding isatin-based Schiff base derivatives, which qualify them for use in polyester textiles.[20] For isatin-containing azo compounds to retain dye integrity during manufacturing and use, their thermal and storage stability is crucial.[21] Improved color strength and fastness are directly linked to these stability parameters, ensuring resistance to degradation at high dyeing temperatures and long-term color retention.[22] Recent developments in computational chemistry, coupled with knowledge of biological and metabolic mechanisms and structures, have resulted in the creation of an extensive companion.[23] It has made a substantial contribution to our knowledge of the structure, properties, and selectivity of molecules.[24] Furthermore, it furnishes us with crucial particulars concerning the compounds under investigation, including total energy, dipole moment, electronic energy, binding energy, LUMO, HOMO, and bond lengths. When this data is in line with the experiment's results, its value increases. Additionally, it helps us understand how the molecule would most likely behave during reactions.[25] The most promising method for using computer-based computations to investigate the electrochemical properties of different substances is density functional theory (DFT).[24–26] In comparison to other existing methodologies, Density Functional Theory (DFT) is inexpensive and provides an excellent level of accuracy with less computational time.[26,27] Considering these factors, we aimed to design and synthesize a novel class of isatin-based azo dyes and to evaluate their anti-inflammatory potential. DFT studies were employed to examine how electronic and molecular structural modifications influence biological activity. The development of disperse dyes that combine commercial dyeing performance with biological functionality has recently attracted significant attention.[28,29] A basic biological reaction to an infection or damage, inflammation, is linked to many illnesses, such as cancer, autoimmune diseases, and heart failure. During the inflammatory process, mediators such as interleukins (IL-2, IL-6) and tumor necrosis factor-alpha (TNF-α) are released, along with activation of cyclooxygenase (COX-1/2) enzymes.[30,31] Lipopolysaccharide (LPS), a bacterial endotoxin, is widely used in experimental inflammation models, as it triggers proinflammatory pathways in macrophages, leading to increased expression of cytokines and mediators such as IL-6, TNF-α, COX-2, and nitric oxide (NO).[32,33] Suppressing these mediators is therefore a key therapeutic approach in managing inflammatory disorders. Combining azo dyes with isatin-based Schiff base moieties provides an innovative route to achieve both functional finishing and dyeing in a single step. Even in the absence of substantial medicine release, fabrics printed with anti-inflammatory dye molecules can offer significant functional benefits at the skin-textile interface. Surface-bound bioactive moieties (such as isatin-based azo dyes) can indirectly reduce skin irritation, odor, and discomfort by influencing microbial growth, oxidative stress, and local inflammatory responses through continuous contact between textiles and the skin, especially during prolonged or humid wear conditions. This function is particularly important for advanced and medical textiles, as materials that come into contact with delicate or injured skin have been demonstrated to reduce inflammation and promote healing when bioactive components are present at the surface. As part of the new idea of "biofunctional colorants", which combine colors with latent biological activity, adding anti-inflammatory structures is still beneficial from a scientific standpoint, even in traditional polyester systems where dyes are mostly immobilized inside the fiber. As a result, these textiles increase wearer comfort and hygiene and offer an attractive option for the development of bioactive textile systems with multiple functions and regulated release in the future.[34–36] This work presents the first report on synthesizing isatin–Schiff base bioconjugates linked through an azo bridge. These novel compounds are explored as disperse dyes for polyester printing, with additional evaluation of their anti-inflammatory activities.

Experimental

Chemicals and instrumentation

All reagents and starting materials are discussed in the SI. All instruments and methods were observed in the SI section.

Purity and characterization

All compounds were separated after completion of the reaction using thin layer chromatography (TLC: ethyl acetate: petroleum ether 1 : 3). The purity of all synthesized compounds was achieved *via* flash column chromatography and confirmed *via* different characterization methods, including elemental analysis, FT-IR, ^{1}H-NMR, and ^{13}C-NMR.

Organic synthesis

General method for the synthesis of 2-cyano-2-(2-oxoindolin-3-ylidene) acetohydrazide. 2-Cyano-2-(2-oxoindolin-3-ylidene) acetohydrazide was synthesized according to the literature.[34]

General method for the synthesis of Schiff base compounds 2 and 3. A mixture of 2-cyano-2-(2-oxoindolin-3-ylidene) acetohydrazide[37] (**1**) (2.28 g, 10 mmol) and an ethanolic solution of aromatic aldehyde (10 mmol) in a few drops of acetic acid was refluxed for 6–8 h (TLC control: ethyl acetate: petroleum ether 1 : 3). The reaction mixture was poured into ice water, filtered off, dried, and recrystallized from ethanol.

2-Cyano-*N*′-((*E*)-4-hydroxy-3-methoxybenzylidene)-2-((*Z*)-2-oxoindolin-3-ylidene) acetohydrazide (2). Orange red solid, yield 89%; mp 210 °C; ^{1}H NMR (400 MHz, DMSO-d$_6$) δ (ppm): 10.82

(s, 1H, CONH), 10.52 (s, 1H, NH-indole), 9.70 (s, 1H, OH), 8.53 (s, 1H, CH=N), 6.87–8.05 (m, 7H, Ar–H), 3.85 (s, 3H, OCH_3); ^{13}C NMR (101 MHz, DMSO-d_6) δ (ppm): 165.40 (C=O indole), 163.32 (C=O), 152.01 (C–OH), 148.70 (C–OCH_3), 110.00 (CN), 100.00 (CH=N), 56.20 (O–CH_3), 111.20–145.20 (Ar–C); IR (KBr) ν: 3459.47 (OH), 3413.90 (NH), 3286.31 (CH-arom), 3022.00 (CH-aliph), 2359.49 (C≡N), 1714.50 (C=O), 1657.20 (C=N), 1605.14 (C=C); Anal. Calcd for $C_{19}H_{14}N_4O_4$ (362.34): C, 62.98%; H, 3.89%; N, 15.46%. Found: C, 62.58%; H, 3.69%; N, 15.28%.

2-Cyano-*N*′-((*E*)-3,5-dimethoxybenzylidene)-2-((*Z*)-2-oxoindolin-3-ylidene)acetohydrazide (3). Deep yellow solid, yield 90%; mp 143 °C; ^1H NMR (400 MHz, DMSO-d_6) δ (ppm): 10.65 (s, 1H, CONH), 10.52 (s, 1H, NH-indole), 8.61 (s, 1H, CH=N), 6.62–8.44 (m, 7H, Ar–H), 3.80 (s, 6H, 2OCH_3); ^{13}C NMR (101 MHz, DMSO-d_6) δ (ppm): 161.45 (C=O indole), 161.24 (C=O), 159.25 (C–OCH_3), 104.58 (CN), 56.01 (O–CH_3), 106.60–136.10 (Ar–C); IR (KBr) ν: 3356.42 (OH), 3283.51 (NH), 3210.59 (CH-arom), 3092.11 (CH-aliph), 2286.58 (C≡N), 1720.82 (C=O), 1663.33 (C=N), 1593.92 (C=C); Anal. Calcd for $C_{20}H_{16}N_4O_4$ (376.37): C, 63.83%; H, 4.29%; N, 14.89%. Found: C, 63.53%; H, 4.17%; N, 14.63%.

General method for the synthesis of isatin azodyes (4a–d). A cooled sodium nitrite solution (0.90 g, 12.7 mmol) in water was added dropwise to a cooled solution of aromatic amine (13.7 mmol) dissolved in concentrated HCl. The diazonium salt was then added dropwise to a cooled solution of compound 2 (3.07 g, 8.5 mmol) dissolved in 10 mL (10% NaOH). The reaction mixture was stirred overnight at 0 °C, the product was filtered, crystallized from ethanol, and dried to offer compounds **4a–d**.

2-Cyano-*N*′-((*E*)-4-hydroxy-3-methoxy-5-((*E*)-(4-nitrophenyl) diazenyl) benzylidene)-2-((*Z*)-2-oxoindolin-3-ylidene) acetohydrazide (4a). Orange red dye; yield 91%; mp 120–122 °C; ^1H NMR (400 MHz, DMSO-d_6) δ (ppm): 11.00 (s, 1H, CONH), 10.81 (s, 1H, NH-indole), 9.72 (s, 1H, OH), 8.54 (s, 1H, CH=N), 6.88–8.16 (m, 10H, Ar–H), 3.90 (s, 3H, OCH_3); ^{13}C NMR (101 MHz, DMSO-d_6) δ (ppm): 165.38 (C=O indole), 163.96 (C=O), 163.00 (C–OH), 151.82 (C–OCH_3), 116.50 (CN), 110.00 (CH=N), 56.45 (O–CH_3), 120.50–148.70 (Ar–C); IR (KBr) ν: 3320.66 (NH/OH), 3120.15 (CH-arom), 3083.70 (CH-aliph), 2124.00 (C≡N), 1720.81 (C=O), 1668.93 (C=N), 1605.84 (C=C), 1457.91 (N=N); Anal. Calcd for $C_{25}H_{17}N_7O_6$ (511.45): C, 58.71%; H, 3.35%; N, 19.17%. Found: C, 58.51%; H, 3.17%; N, 19.03%.

2-Cyano-*N*′-((*E*)-4-hydroxy-3-((*E*)-(4-hydroxyphenyl)diazenyl)-5-methoxybenzylidene)-2-((*Z*)-2-oxoindolin-3-ylidene) acetohydrazide (4b). Dark brown; yield 92%; mp 130–132 °C; ^1H NMR (400 MHz, DMSO-d_6) δ (ppm): 10.98 (s, 1H, CONH), 10.80 (s, 1H, NH-indole), 10.03 (s, 1H, OH), 9.74 (s, 1H, OH), 8.53 (s, 1H, CH=N), 6.86–8.04 (m, 10H, Ar–H), 3.85 (s, 3H, OCH_3); ^{13}C NMR (101 MHz, DMSO-d_6) δ (ppm): 165.40 (C=O indole), 163.98 (C=O), 163.30 (C–OH), 151.77 (C–OCH_3), 116.30 (CN), 110.20 (CH=N), 56.21 (O–CH_3), 116.30–148.70 (Ar–C); IR (KBr) ν: 3419.51 (NH/OH), 3142.12 (CH-arom), 3081.59 (CH-aliph), 2102.90 (C≡N), 1727.13 (C=O), 1665.43 (C=N), 1610.04 (C=C), 1457.91 (N=N); Anal. Calcd for $C_{25}H_{18}N_6O_5$ (482.46): C, 62.24%; H, 3.76%; N, 17.42%. Found: C, 62.14%; H, 3.66%; N, 17.36%.

2-Cyano-*N*′-((*E*)-4-hydroxy-3-methoxy-5-((*E*)-(4-methoxyphenyl)diazenyl)benzylidene)-2-((*Z*)-2-oxoindolin-3-ylidene) acetohydrazide (4c). Dark red dye; yield 89%; mp 105–107 °C; ^1H NMR (400 MHz, DMSO-d_6) δ (ppm): 11.01 (s, 1H, CONH), 10.81 (s, 1H, NH-indole), 9.73 (s, 1H, OH), 8.53 (s, 1H, CH=N), 6.82–8.05 (m, 10H, Ar–H), 3.85 (s, 3H, OCH_3), 3.80 (s, 3H, OCH_3); ^{13}C NMR (101 MHz, DMSO-d_6) δ (ppm): 165.39 (C=O indole), 163.20 (C=O), 162.97 (C–OH), 151.80 (C–OCH_3), 110.50 (CN), 100.00 (CH=N), 56.20 (O–CH_3), 110.50–151.06 (Ar–C); IR (KBr) ν: 3342.39 (NH/OH), 3151.01 (CH-arom), 3078.09 (CH-aliph), 2100.79 (C≡N), 1720.81 (C=O), 1665.43 (C=N), 1610.75 (C=C), 1454.41 (N=N); Anal. Calcd for $C_{26}H_{20}N_6O_5$ (496.48): C, 62.90%; H, 4.06%; N, 16.93%. Found: C, 62. 39%; H, 3.86%; N, 16.75%.

2-Cyano-*N*′-((*E*)-4-hydroxy-3-methoxy-5-((*E*)-phenyldiazenyl) benzylidene)-2-((*Z*)-2-oxoindolin-3-ylidene)acetohydrazide (4d). Orange red dye; yield 90%; mp 140–142 °C; ^1H NMR (400 MHz, DMSO-d_6) δ (ppm): 12.65 (s, 1H, CONH), 11.20 (s, 1H, NH-indole), 9.72 (s, 1H, OH), 8.53 (s, 1H, CH=N), 6.84–8.04 (m, 11H, Ar–H), 3.85 (s, 3H, OCH_3); ^{13}C NMR (101 MHz, DMSO-d_6) δ (ppm): 165.40 (C=O indole), 163.99 (C=O), 162.90 (C–OH), 151.78 (C–OCH_3), 112.29 (CN), 100.00 (CH=N), 56.22 (O–CH_3), 112.29–148.70 (Ar–C); IR (KBr) ν: 3339.59 (NH/OH), 3114.57 (CH-arom), 3078.09 (CH-aliph), 2158.98 (C≡N), 1720.81 (C=O), 1666.13 (C=N), 1613.55 (C=C), 1460.72 (N=N); Anal. Calcd for $C_{25}H_{18}N_6O_4$ (466.46): C, 64.37%; H, 3.89%; N, 18.02%. Found: C, 64.23%; H, 3.69%; N, 17.46%.

General method for the synthesis of azo compounds (5a–d). A mixture of sodium nitrite (0.90 g, 12.7 mmol) in water was added dropwise to a cooled solution of aromatic amine (13.7 mmol) dissolved in concentrated HCl. The diazonium salt was then added dropwise to a cooled solution of compound 3 (3.19 g, 8.5 mmol) dissolved in 10 mL pyridine. The reaction mixture was stirred overnight at 0 °C, the product was filtered, crystallized from ethanol, and dried to offer compounds **5a–d**.

(*Z*,*Z*)-5-(2-cyano-2-((*Z*)-2-oxoindolin-3-ylidene)acetyl)-3-(3,5-dimethoxyphenyl)-1-(4-nitrophenyl)formazan (5a). Orange red dye; yield 90%; mp 80–82 °C; ^1H NMR (400 MHz, DMSO-d_6) δ (ppm): 10.98 (s, 1H, CONH), 10.86 (s, 1H, NH-indole), 6.60–8.59 (m, 11H, Ar–H), 3.76 (s, 6H, 2OCH_3); ^{13}C NMR (101 MHz, DMSO-d_6) δ (ppm): 161.45 (C=O indole), 161.24 (C=O), 159.25 (C–OCH_3), 104.58 (CN), 56.01 (O–CH_3), 106.62 -150.46 (Ar–C); IR (KBr) ν: 3421.61 (NH/OH), 3281.40 (CH-arom), 3087.21 (CH-aliph), 2354.59 (C≡N), 1720.82 (C=O), 1668.93 (C=N), 1593.92 (C=C), 1454.41 (N=N); Anal. Calcd for $C_{26}H_{19}N_7O_6$ (525.48): C, 59.43%; H, 3.64%; N, 18.66%. Found: C, 59. 29%; H, 3.44%; N, 18.48%.

(*Z*,*Z*)-5-(2-Cyano-2-((*Z*)-2-oxoindolin-3-ylidene)acetyl)-3-(3,5-dimethoxyphenyl)-1-(4-hydroxyphenyl)formazan (5b). Dark brown dye; yield 91%; mp 145–147 °C; ^1H NMR (400 MHz, DMSO-d_6) δ (ppm): 11.01 (s, 1H, CONH), 10.88 (s, 1H, NH-indole), 10.67 (s, 1H, OH), 6.61–8.80 (m, 11H, Ar–H), 3.77 (s, 6H, 2OCH_3); ^{13}C NMR (101 MHz, DMSO-d_6) δ (ppm): 161.93 (C=O indole), 161.43 (C=O), 161.23 (C–OCH_3), 104.08 (CN), 56.00 (O–CH_3), 106.64–145.77 (Ar–C); IR (KBr) ν: 3404.09 (NH/OH), 3284.20 (CH-arom), 3092.81 (CH-aliph), 2218.06 (C≡N),

1725.58 (C=O), 1669.76 (C=N), 1597.54 (C=C), 1463.74 (N=N); Anal. Calcd for $C_{26}H_{20}N_6O_5$ (496.48): C, 62.90%; H, 4.06%; N, 16.93%. Found: C, 62. 69%; H, 3.96%; N, 16.85%.

(*Z*,*Z*)-5-(2-Cyano-2-((*Z*)-2-oxoindolin-3-ylidene)acetyl)-3-(3,5-dimethoxyphenyl)-1-(4-methoxyphenyl)formazan (5c). Light brown dye; yield 92%; mp 155–157 °C; ^{1}H NMR (400 MHz, DMSO-d_6) δ (ppm): 11.02 (s, 1H, CONH), 10.87 (s, 1H, NH-indole), 6.61–8.60 (m, 11H, Ar–H), 3.79 (s, 6H, 2OCH$_3$), 3.76 (s, 3H, OCH$_3$); ^{13}C NMR (101 MHz, DMSO-d_6) δ (ppm): 161.92 (C=O indole), 161.42 (C=O), 159.22–161.22 (C–OCH$_3$), 104.07 (CN), 55.99 (O–CH$_3$), 106.64–149.48 (Ar–C); IR (KBr) ν: 3356.42 (NH/OH), 3155.91 (CH-arom), 3082.99 (CH-aliph), 2089.58 (C≡N), 1725.02 (C=O), 1679.45 (C=N), 1588.32 (C=C), 1460.72 (N=N); Anal. Calcd for $C_{27}H_{22}N_6O_5$ (510.51): C, 63.52%; H, 4.34%; N, 16.46%. Found: C, 63. 36%; H, 4.22%; N, 16.28%.

(*Z*,*Z*)-5-(2-Cyano-2-((*Z*)-2-oxoindolin-3-ylidene)acetyl)-3-(3,5-dimethoxyphenyl)-1-phenylformazan (5d). Dark red dye; yield 91%; mp 100–102 °C; ^{1}H NMR (400 MHz, DMSO-d_6) δ (ppm): 10.99 (s, 1H, CONH), 10.88 (s, 1H, NH-indole), 6.61–8.90 (m, 12H, Ar–H), 3.76 (s, 6H, 2OCH$_3$); ^{13}C NMR (101 MHz, DMSO-d_6) δ (ppm): 161.43 (C=O indole), 161.23 (C=O), 161.23 (C–OCH$_3$), 104.09 (CN), 56.00 (O–CH$_3$), 106.64–148.90 (Ar–C); IR (KBr) ν: 3396.37 (NH/OH), 3219.00 (CH-arom), 3091.41 (CH-aliph), 2164.70 (C≡N), 1725.58 (C=O), 1680.43 (C=N), 1592.61 (C=C), 1460.46 (N=N); Anal. Calcd for $C_{26}H_{20}N_6O_5$ (480.15): C, 64.99%; H, 4.20%; N, 17.49%. Found: C, 64. 79%; H, 4.06%; N, 17.27%.

Printing and fastness determination

Printing paste procedure

To prepare each printing paste dye, Table 1 lists the quantities of all ingredients used in the preparation of the printing paste. Polyester fabric samples were printed using the aforementioned printing paste *via* the traditional screen-printing method. Following a period of drying at room temperature, the prints were thermo-fixed for four minutes at 180 °C. When fabrics were being thermofixed, they were simultaneously stretched (tensioned) and heated.[6] After being stretched between a metal holder, the textile samples are placed in an automatic thermostatic oven (Fyianyuan Instrument Co., model number LD-3642, China) and baked for 4 min at 180 °C. Several methods are used to wash the prints, including two cold–water cycles, two hot–water cycles, 20 minutes at 60 °C, and 2 g of nonionic detergent per liter.[6]

Table 1 The amounts used to make the printing paste ingredients

Component	Amount	Function
Dye	3 g	Colorant
Thickener	75 g	Rheology modifier
Lyoprint EV (dispersing agent)	0.5 g	Dye dispersing agent
Acetic acid	0.5–1 g	pH adjustment (pH 5–6)
Water	21 g	Solvent/medium
Total	100 g	

Color strength measurements (*K*/*S*) and analyses

A Hunter Lab Ultra Scan PRO spectrophotometer was used to assess the colorimetric strength data after the printed polyester fabric samples had been washed and dried. The basis for measuring the printed samples, at least at the dye concentration of the paste, is the notion that (*K*/*S*) values are proportionate to the dye concentration on the fabric under printed conditions.[2] The color strength, expressed by the *K*/*S* value, was determined using the Kubelka–Munk eqn (1).

$$K/S = \frac{(1-R)^2}{2R} \quad (1)$$

R = Decimal fraction of the dyed fabric reflection, K = absorption coefficient, and S = scattering coefficient. Because it influences consumer demand and tastes, the color of printed fabrics is important. The color characteristics of the surfaces of printed polyester fabrics were evaluated by examining colorimetric data for printed fabrics in terms of L^*, a^*, and b^* using the CIELAB system.[2]

Fastness properties methods

In accordance with the standard method ISO 105-C06 B2S (2012), the wash fastness test was performed using a mixture of 4 g L^{-1} ECE detergent, 1 g L^{-1} sodium perborate, and 25 steel balls at 50 °C for 30 minutes, with a liquor ratio of 50 : 1. The colored polyester fabric was placed on the crockmeter's base so that its long dimension in the direction of rubbing sat flat on the sharp fabric. The ISO 105-X12:2001 rubbing fastness test was carried out in that way. A square of white testing fabric was allowed to glide on the tested fabric twenty times by turning the crank ten full turns. The testing squares were completely submerged in distilled water for the wet rubbing test. The remainder of the process was identical to that of the dry test. The white testing fabric's degradation was assessed using a grayscale, with 1 denoting poor, 2 fair, 3 moderate, 4 acceptable, and 5 excellent. The fastness to acidic and alkaline perspiration was measured using a perspiromete set at a specific pressure, temperature, and time in accordance with ISO 105-E04, and any color shift of the dyed samples (Alt) and color staining on the nearby undyed cotton (SC) and polyester (SP) fabrics were then evaluated using the related ISO grey scales for color change and staining rates. Light fastness was further assessed using a Xenon arc lamp test in accordance with ISO 105-B02. The dry heat fastness test was conducted at 180 or 210 °C using a fixometer in accordance with ISO 105-P01. Any change in the specimens' color (Alt) and any color staining of the surrounding cotton (SC) and polyester (SP) were then assessed using the corresponding ISO greyscales for color change and staining.[38–41]

Assessment of anti-inflammatory activity of the synthesized dyes

Cell culture (seeding and treatment)

The RAW 264.7 macrophage cell line was maintained in DMEM-F12 medium. The media was supplemented with 10% fetal

bovine serum at 37 °C in 5% CO_2 and 95% humidity. Cells were subcultured using 0.15% trypsin. The cell line was kindly provided by Professor Stig Linder, the Oncology and Pathology Department, Karolinska Institute, Stockholm, Sweden, and was originally obtained from ATCC.[30–33,42]

Cell viability assay

The viability of the RAW 264.7 macrophage cell line was determined following the method of Elshahid *et al.*[30] with slight modifications. Briefly, after 24 h of seeding (5×10^5 cells per well), cells were treated with a final concentration of 100 μg mL^{-1} of isatin derivatives and celecoxib in triplicate for 24 h. Doxorubicin (positive control) was applied at a concentration of 100 μM, and DMSO (negative control) at 0.5% concentration. The viability was estimated by the reduction of yellow MTT (3-(4,5-dimethylthiazol-2-yl)-2,5-diphenyltetrazolium bromide) to purple formazan as described previously. Viability % was calculated as follows:

$$\%\ \text{Viability} = ((\text{OD} - X/\text{OD} - \text{NC}) - 1) \times 100$$

where OD: optical density, X: absorbance of sample well, NC: absorbance of negative control measured at 595 nm with reference at 690 nm.

Nitric oxide assay

The effect of isatin derivatives on nitric oxide (NO) levels was determined in RAW 264.7 cells according to the method of Hamed *et al.*[31] with slight modifications. Cells were pre-incubated with various concentrations (100, 50, 25, 12.5 μg mL^{-1}) of isatin analogues for 1 hour, then treated with LPS (100 ng mL^{-1}) for 24 hours. The release of nitrite in culture supernatants was recorded as a marker of NO production and measured by the Griess test. Briefly, 100 μL of culture supernatant was collected at the end of incubation, mixed with an equal volume of Griess reagent, and incubated at room temperature for 10 minutes. Absorbance at 540 nm was recorded, and a sodium nitrite standard curve was used to calculate the amount of nitrite, as shown in the equation:

$$\text{Nitric oxide inhibition}(\%) = \frac{(\text{control} - \text{test})}{\text{control}} \times\ 100$$

Effect of isatin derivatives on TNF-α and IL-6 and cyclooxygenase (COX-2) levels in mouse macrophages

The *in vitro* anti-inflammatory activity of isatin derivatives was determined in RAW 264.7 cells according to the method of, with slight modifications: cells were pretreated with different concentrations of isatin derivatives for 1 hour, then incubated with LPS (100 ng mL^{-1}) for 24 hours. The inflammatory mediator's interleukin-6 (IL-6), tumor necrosis factor (TNF-α), and cyclooxygenase (COX-2) were assessed using a Sunlong Biotech Co., Ltd, China ELISA (Enzyme-Linked Immunosorbent Assay) kit. The manufacturer's instructions of the kit were followed, to estimate the results. Samples and standards were pipetted into the wells with antibodies specific for Il-6 and TNF-α and COX-2 then were incubated. After incubation, the wells were washed away, and horseradish peroxidase-conjugated streptavidin was pipetted into the wells, which were washed once again. TMB (tetramethylbenzidine) substrate solution was added to the wells; color developed proportionally to TNF-α, Il-6 and COX-2 bound amount. Color development was discontinued (stop solution) and the color intensity was measured at 450 nm.[43]

Statistical analysis

All statistical analysis and IC_{50} values were calculated using the concentration-response curve fit to the non-linear regression model and One-way ANOVA was performed using GraphPad Prism® v6.0 (GraphPad Software Inc., San Diego, CA, USA).

Results and discussion

Vanillin and/or 3,5-dimethoxy benzaldehyde, respectively, interacted with 2-cyano-2-(2-oxoindolin-3-ylidene) acetohydrazide (**1**)[37] in ethanol and drops of acetic acid to produce two distinct Schiff bases of isatin derivatives **2** and **3**, Scheme 1.

Compounds **2** and **3** were confirmed with different spectroscopic data (IR and NMR). The FT-IR spectra revealed different absorption bands at 3400 cm^{-1} for NH/OH, 3280–3155 cm^{-1} for Ar–H, 2300 cm^{-1} for C≡N, 1725 cm^{-1} for C=O, and 1650 cm^{-1} for C=N, Fig. S1 and S2. The ^{1}H-NMR spectra of compounds **2** and **3** revealed different signals at 3.80 ppm, 8.55 ppm, 10.50 ppm, and 10.70 ppm due to OCH_3, CH=N Schiff base, NHindole, and NH_{amide} protons, respectively, Fig. S3–S5. ^{13}C-NMR (DMSO) analysis of **2** shows the following signals: δ 56.21 (OCH_3), 109.84 ($HC{=}N_{Sciff\ base}$), 151.96 (C–OCH_3), 163.23, 165.39 (C=O), and 110.51–149.01 ($C_{Arom.}$), Fig. S6.

^{13}C-NMR (DMSO) analysis of the compound **3** shows the following signals: δ 56.01 (2 OCH_3), 104.58 ($HC{=}N_{Sciff\ base}$), 159.25 (C–OCH_3), 161.24, 161.45 (C=O), and 106.60–134.49 ($C_{Arom.}$), Fig. S7.

The diazotization of different aromatic amines was performed to produce the corresponding diazonium salt which couples with the sodium salt of Schiff's bases (**2** and **3**) to give 2-cyano-*N*′-(4-hydroxy-3-methoxy-5-((*E*)-(Aryl)diazenyl)benzylidene)-2-((*Z*)-2-oxoindolin-3-ylidene)acetohydrazide (**4a–d**) and (*E*)-5-(2-cyano-2-((*Z*)-2-oxoindolin-3-ylidene)acetyl)-3-(3,5-dimethoxyphenyl)-1-(Aryl)formazan (**5a–d**), respectively, Schemes 2 and 3.

The FT-IR spectra of compounds **4a–d** showed different absorption bands for the N=N, C=C, C=N, C=O, C≡N, and NH/OH groups at 1454–1460 cm^{-1}, 1605–1613 cm^{-1}, 1665–1668 cm^{-1}, 1720 cm^{-1}, 2100–2158 cm^{-1}, and 3339 and 3419 cm^{-1}, respectively, Fig. S1.

The FT-IR spectra of compounds **5a–d** showed different absorption bands for the N=N, C=C, C=N, C=O, C≡N, and NH/OH groups at 1440 cm^{-1}, 1593–1680 cm^{-1}, 16597–1668 cm^{-1}, 1725 cm^{-1}, 2089–2354 cm^{-1}, and 3356 and 3421 cm^{-1} respectively, Fig. S2. The ^{1}H-NMR spectra of compounds **4a–d** revealed different signals at 3.80–3.85 ppm, 8.53 ppm, 9.72–10.03 ppm, and 11.00 ppm due to OCH_3, CH=N, OH, and NH_{indole} protons, respectively, Fig. S8–S11. The ^{1}H-NMR spectra of compounds **5a–d** revealed important signals at

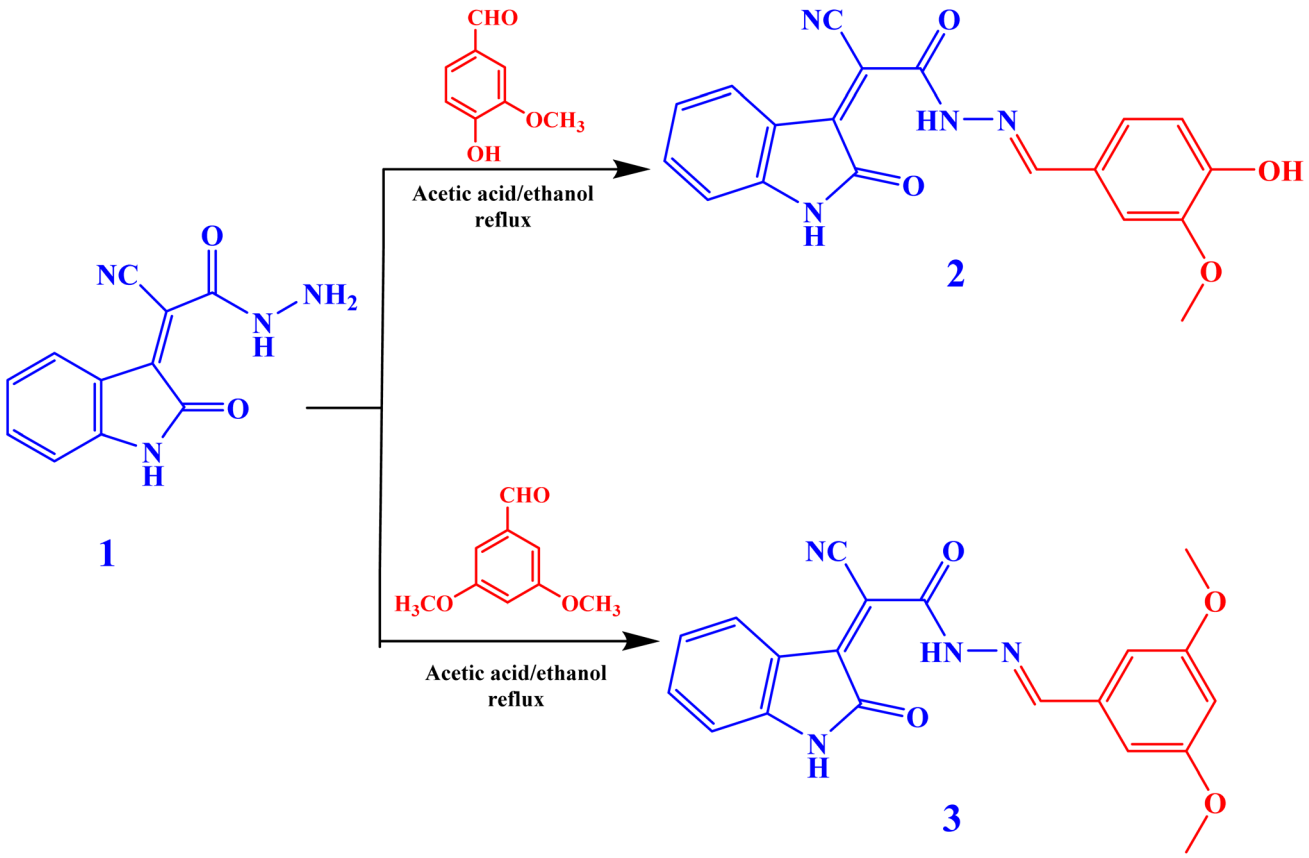

Scheme 1 Synthetic pathway of Schiff bases of isatin compounds 2 and 3.

3.76–3.79 ppm, 10.88 ppm, and 11.00 ppm due to $2OCH_3$, NH_{indole}, and CONH protons respectively, Fig. S12–S15. ^{13}C-NMR (DMSO) analysis of **4a–4d** shows the following signals: δ 56 (OCH_3), 110 ($HC{=}N_{Sciff\ base}$), 151 (C–OCH_3), 153, 165 (C=O), and 110–151 ($C_{Arom.}$), Fig. S16–S19. ^{13}C-NMR (DMSO) analysis of **5a–5d** shows the following signals: δ 56 (OCH_3), 104 (CN), 159 (C–OCH_3), 161 (C=O), and 106–149 ($C_{Arom.}$), Fig. S20–S23 SI.

Color performance of azo disperse dyes on polyester fabric

Test prints performed with new synthetic dyes must be made in order to determine whether dye derivatives are appropriate as azo disperse dyes for printing polyester fabric at a concentration of 3 wt% mixed with printing paste. This was achieved through making a range of printing pastes that were thickened using synthetic thickeners and yielded acceptable results. The new azo dyes were utilized to produce pastes for printing on polyester fabric. Colloidal coloring was used to generate polyester fabrics with a highly uniform yellow print that came in a range of colors (yellow, greenish yellow and brownish yellow). The color tones of the dyed fabrics are shown in Table 2 along with the color intensity (represented as K/S) of the screen-printed dyes applied to polyester. Different print values are produced by the K/S values, which are influenced by the kind and chemical structure of the new dyes. The presence of conjugated double bonds, the dye molecule's planarity, and its linearity are the main characteristics that contribute to better dye fixation. Additionally, substituent location is quite important. Since the hydroxyl group on the dye is an auxochrome, which enhances the dye color and increases the conjugated double bond. The electron-withdrawing nitro group (–NO_2), which promotes bathochromic and hyperchromic effects and improves tinctorial strength by increasing π-electron delocalization across the azo chromophore, is responsible for the increased color strength observed for dye **4a**. On the other hand, the dye structure (**4a–d**) naturally contains the hydroxyl group (–OH), which functions as an auxochrome to increase color intensity and enhance intermolecular interactions with the polyester substrate, such as hydrogen bonding and dipole–dipole interactions. These substituent effects are well known in azo disperse dye systems, where hydroxyl groups improve dye–fiber affinity and overall dyeing efficiency while electron-withdrawing groups improve range characteristics and color strength,[44,45] Table 2. The following formulas were used to determine the hue angle (h°) and chroma (saturation) (C^*):[46]

$$C^* = \sqrt{(a^*)2 + (b^*)2} \quad (2)$$

$$h^\circ = \tan^{-1}\left(\frac{b^*}{a^*}\right) \quad (3)$$

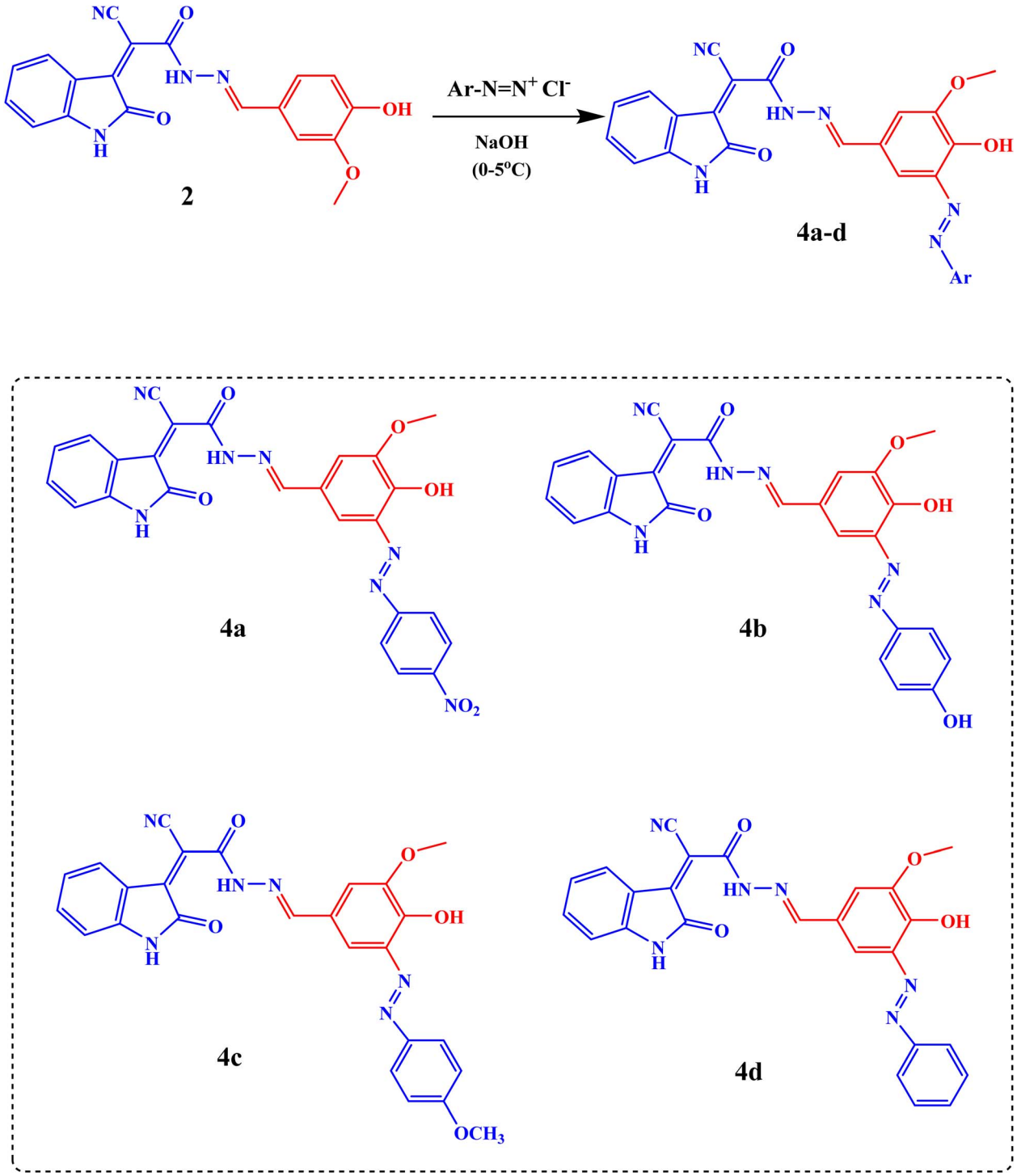

Scheme 2 Synthesis of compounds **4a–d**.

The recently developed isatin Schiff base dyes' blackness or lightness on polyester materials is determined by comparing the L^* and C^* values. The dyes **4a–d** and **5a–d** have color lightness values (L^*) ranging from 48.67 to 71.56. The dyes **4c**, **4d**, and **5d** are lighter compared with the other dyes. All the synthesized dyes give a redder tone (positive a^* values and a yellower tone (positive b^* values).

Fastness properties

Washing fastness

The ability of colored materials to retain their color after being washed with soap and detergent is referred to as "wash fastness". The traditional gray scale is used to grade color variations in dyed molecules and stains on the white area of the printed

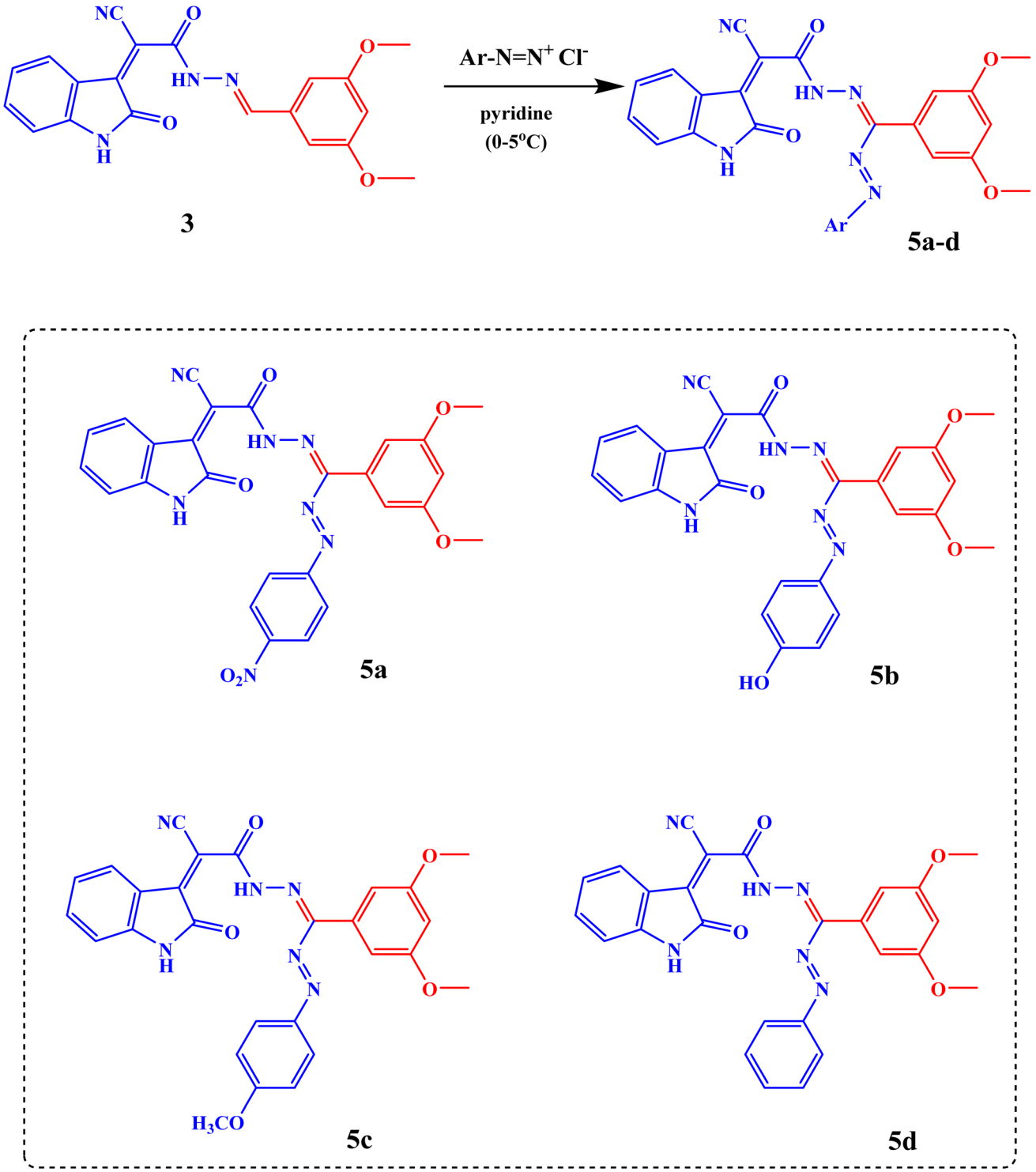

Scheme 3 Synthesis of compounds 5a–d.

fabric. Polyester fabric's washing fastness was evaluated by measuring how quickly the synthesized dyes were extracted from the fabric after washing. The dye's molecular size, water solubility, and mechanical contact type with the fabric were among the several variables. It is well-known that the wash fastness increases with the size of the dispersed dye. Thus, it is conceivable that larger molecules can be used to create dispersion dyes with minimal thermo-migration. The unlevel dyeing caused by the limited dye uptake and greater fiber-dye interplay because of the decreased mobility are the expected weak points in this specific case.[47] Excellent washing fastness has been shown by the printed polyester fabrics tested with dyes

Table 2 Azo disperse dyes **4a–d** and **5a–d** printed on polyester fabrics: optical measurements[a]

Dye	Color shade	Photo of printed sample	Absorption [λ_{max} (nm)] on fabrics	*K*/*S*	*L**	*a**	*b**	*C**	*h*
4a	Brown		395	14.79	48.67	13.10	42.23	44.22	72.77
4b	Yellow		390	11.30	69.19	8.33	32.73	32.78	86.70
4c	Yellow		390	11.80	70.62	1.89	18.57	20.36	65.83
4d	Orange yellow		375	9.18	71.56	1.63	42.75	42.78	87.81
5a	Yellow		390	12.09	62.66	1.93	53.80	53.84	87.94
5b	Brownish yellow		380	10.64	68.44	0.30	29.04	29.04	89.41
5c	Yellow		385	11.33	66.80	3.25	45.20	45.32	85.88
5d	Dark yellow		375	8.97	69.19	1.89	32.73	32.78	86.70

[a] Lightness (*L**), degree of redness (+ve) and greenness (−ve) (*a**), degree of yellowness (+ve) and blueness (−ve) (*b**), chroma (*c**), hue (*h*) and color strength (*K*/*S*).

4a, **5a**, and **5b**; washing fastness is good for the remaining dyes, Table 3. The dye-fiber affinity and insufficient dye molecule consumption in the fabrics are the causes of this.

Acid and alkaline fastness to perspiration

Regardless of pH level, the majority of colored materials received high ratings for perspiration fastness, suggesting that pH has little effect on the dyed samples' sensitivity. This may be explained by the innate ability to withstand deterioration in both basic and alkaline conditions. The grayscale was used to assess the color comparisons. The dye-printed polyester fabric produced very good to outstanding (4–5) outcomes, Table 3.

Rubbing fastness

The ability of a fabric to keep its color when exposed to the abrasive forces of rubbing at a particular pressure is known as color fastness to rubbing. A reactive (dry/wet) white cotton fabric is used in the color fastness to rubbing test, a fundamental component of textile quality control, and it is rubbed on the fabric surface a predefined number of times. A standardized grayscale for staining assessment is then used to determine the extent of color transfer to the cotton material. Dry rubbing color fastness, which measures the fabric's resistance to color loss in a dry state, and wet rubbing color fastness, which measures the same in a moist state, are the two main categories into which this attribute is divided. Five was the highest value on a traditional grayscale, and one was the lowest. The dye's molecular weight and the fabric's affinity for the synthetic dye determine how much dye can be obtained from the surface of polyester fabrics. **4a** and **5a** exhibit the least amount of fastness among all the synthetic dyes. Rubbing fastness test results are also shown in Table 3.

Light fastness

Among the most important characteristics to look for in textiles with colors that will be exposed to light in their intended purpose is light fastness. It looks at how long and how well printed dyes hold up against fading when exposed to constant light. The traditional blue scale was used to rate it, with one denoting extremely poor and eight denoting excellent. The degree to which a dye does not deteriorate in the presence of

Table 3 Fastness properties of azo disperse dyes **4a–d** and **5a–d** printed on polyester[a]

	Washing fastness			Rubbing fastness		Perspiration fastness						
						Acidic			Alkali			
	St.					St.			St.			
Sample	SC	SP	Alt.	Dry	Wet	SC	SP	Alt.	SC	SP	Alt.	Light
4a	4–5	3–4	4–5	2–3	2–3	4–5	4	4–5	4–5	4	4	7
4b	3–4	4	3–4	3–4	3–4	4	3–4	3–4	3–4	4	3–4	6
4c	4	4	3–4	3–4	3–4	3–4	4	4–5	4–5	3–4	4	7
4d	3–4	2–3	2–3	4–5	4–5	3–4	2–3	3–4	3–4	2–3	3–4	5
5a	4–5	4	4–5	2–3	2–3	4–5	4	3–4	4–5	4	4	7
5b	4–5	3–4	4–5	3–4	4	3–4	3–4	4–5	3–4	3–4	4	7
5c	4–5	3–4	4	4	3–4	4	3–4	4	4–5	4–5	4	7
5d	3–4	2–3	2–3	4–5	4–5	3–4	2–3	2–3	3–4	2–3	2–3	5

[a] Fixation of prints was carried out thermo-fixation. Alt, alteration of colour; SC, staining of cotton; SP, staining of polyester. Rate for light fastness: 4–8 (acceptable), 1–3 (not acceptable); rate for different fastness: 3–5 (acceptable), 1–2 (not acceptable).

sunshine is known as its light fastness. These kinds of substituents have a notable effect on the charged particle density around the azo group. For all synthetic dyes, light fastness (5–7) is generally good, as shown in Table 3. Because they can participate in photochemical reactions, dyes containing electron-donating groups and nitro, such as dyes **4a**, **5a**, **4c**, and **5c**, are often more prone to photodegradation. The relative locations of the 4-nitro and 4-methoxy groups in relation to the azo group component and the crystalline form of polyester fiber are likely responsible for the dyes' overall great light fastness.[48]

Sublimation fastness

The sublimation fastness technique was used to estimate the color fastness to sublimation. It shows how resilient the printed dyes are to extreme temperatures and pressure (180 and 210 °C). Every printed dye showed satisfactory results (3–5), Table 4.

Excellent performance on a polyester substrate was demonstrated by the sublimation test results. The large molecular size and the presence of polar substituent groups like –OH, –NH, and NH_2 groups in the benzene rings are the causes of this.[48]

Structure–activity relationship (SAR) for fastness and color strength properties

Molecular structure and dye–fiber interactions within the hydrophobic polyester substrate all influence the color strength (K/S) and fastness properties of the synthesized azo disperse dyes. Dyes with electron-withdrawing groups, such as the nitro substituent ($-NO_2$) found in dye **4a**, show higher K/S values. This occurrence can be explained by increased π-electron delocalization across the azo chromophore, which strengthens light absorption and increases molar absorptivity (hyperchromic effect).[46] Additionally, electron-withdrawing groups improve dipole–dipole interactions with polyester's ester functional groups, increasing molecular polarity and improving dye binding and fixing during thermofixation. On the other hand, dyes with electron-donating groups like hydroxyl (–OH) and methoxy ($-OCH_3$) substituents (such as **4b**, **4c**, and **5b**) displayed moderate K/S values but better intermolecular interactions.[49] As an auxochrome, the –OH group influences molecular aggregation behavior and promotes hydrogen bonding and secondary interactions with the polyester surface. On the opposite hand, high electron donation may impede dye migration into the amorphous parts of polyester fibers by decreasing molecular planarity and π–π stacking efficiency (Fig. 2).

Fastness performance is also significantly influenced by molecular size and planarity. Due to decreased mobility and diffusion out of the fiber matrix, larger and more planar dye molecules (such as **5a** and **5b**) showed better washing and sublimation fastness. This is in line with the free-volume hypothesis of dispersion dyeing, which states that at high temperatures, dye molecules spread into polyester amorphous regions and become physically confined when they cool.[50,51] Fixation stability is further enhanced by strong van der Waals contacts and π–π stacking between the dye molecules and polyester chains. It was found that substituent-induced electronic effects affected light fastness. While electron-withdrawing groups improved resistance to photodegradation

Table 4 Sublimation fastness variables for fabric made from polyester printed with colors **4a–d** and **5a–d** [a]

	Dry heat fastness at 180 °C		Dry heat fastness at 210 °C	
Sample	SC	SP	SC	SP
4a	4–5	4–5	4–5	4
4b	3–4	3–4	3–4	3–4
4c	4	4	4	4
4d	3–4	2–3	3–4	2–3
5a	4–5	4–5	4–5	4
5b	3–4	2–3	3–4	3–4
5c	4–5	4–5	4	4
5d	3–4	2–3	3	2–3

[a] Alt, alteration of color; SC, staining of cotton; SP, staining of polyester.

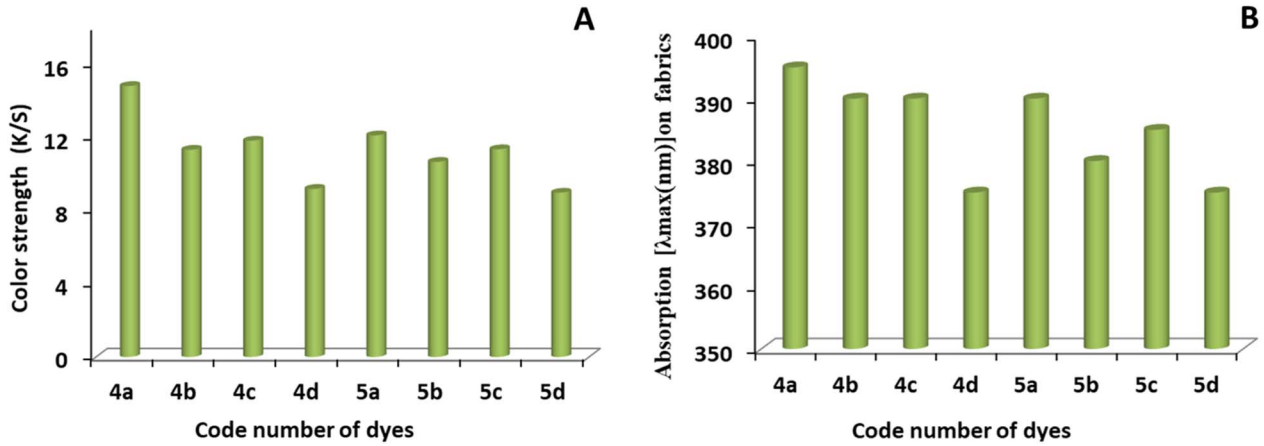

Fig. 2 Colorimetric performances of azo disperse dyes (**4a–5d**) on polyester fabrics: (A) the printed fabrics' color strength (*K*/*S*). (B) The printed fabrics' maximum absorption wavelength (λ_{max}, nm)

by stabilizing the chromophore's excited states, dyes with electron-donating groups showed somewhat decreased photostability because they were more prone to photooxidation. Molecular weight and intermolecular interactions have a significant impact, with larger and more polar dyes exhibiting better resistance to thermal migration.[52] Overall, the combined statistical and molecular analysis makes it abundantly evident that substituent type, electronic distribution, and molecular geometry, all of which together control dye–fiber affinity, diffusion behavior, and fastness properties, have a significant impact on dye performance. These results offer a rational structure to synthesize high-performance disperse dyes for polyester application.

Anti-inflammatory activity

Effect of isatin derivatives on Raw-264.7 macrophages-induced inflammation

Cell viability. As illustrated in Fig. 3, the cytotoxic effects of the synthesized compounds were evaluated using the MTT assay on the tested cell line. The results demonstrated that most of the compounds exhibited negligible cytotoxicity at the tested concentration of 100 μg mL^{-1}, as evidenced by cell viability values comparable to those of the untreated control group.

As illustrated in Fig. 3, compounds **4b** and **5c** showed a noticeable reduction in cell viability at 100 μg mL^{-1}, which suggests a moderate to high cytotoxic effect of them at higher concentrations. In contrast, compounds **4a**, **5a**, and **5d** demonstrated the lowest levels of cytotoxicity among the tested derivatives. These findings indicate that these compounds possess superior biocompatibility and minimal adverse effects on normal cellular metabolism. Their low toxicity makes them particularly promising candidates for further pharmacological evaluation, especially in studies targeting anti-inflammatories.

As illustrated in Table S1, the higher IC_{50} of compounds against normal cells indicates their ability to inhibit cell viability at relatively high concentrations. Also, the IC_{50} values reported for compounds **4b** and **5c** in Table S1 are in good agreement with the cytotoxicity trends observed in Fig. 3. The lower IC_{50} values of compounds **4b** and **5c** against normal cells indicate their ability to inhibit cell viability at relatively low concentrations. This finding reflects higher cytotoxicity, as a reduced IC_{50} value corresponds to increased potency in damaging healthy cells.

Nitric oxide (NO). Nitric oxide production has been linked to macrophage stimulation and inflammatory conditions because of external stimulation.[32] It is used as a marker to assess the anti-inflammatory effects of various compounds.[33] The inhibition of NO release in activated Raw 264.7 macrophages by isatin derivatives is illustrated in Fig. 4. The Raw cells were incubated with both compounds and LPS or LPS only for 24 h. The Griess reagent is used to estimate nitrite release in culture medium. Nitrite is used as a marker of NO levels.

From Fig. 4, most of the evaluated compounds demonstrated comparable inhibitory activities, reducing nitric oxide release by more than 70% relative to untreated and/or LPS-treated control cells. This substantial decrease highlights their effectiveness in attenuating macrophage-mediated inflammatory responses. The quantitative analysis presented in Table S1, which lists the IC_{50} values of the tested compounds, further

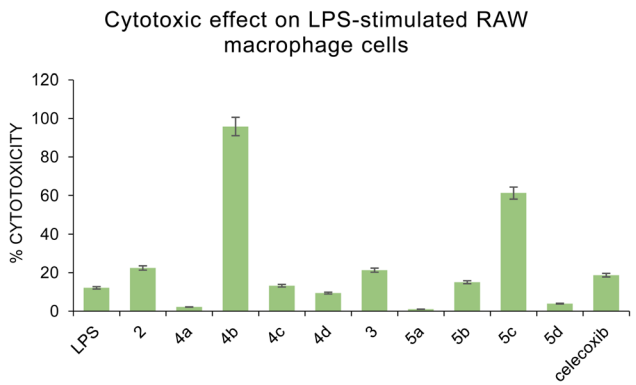

Fig. 3 Effect of isatin derivatives and celecoxib on Raw-264.7 macrophages at 100 μg mL^{-1}. Cells were incubated with different compounds for 24 h. Values are expressed as the means ± SD ($n = 3$).

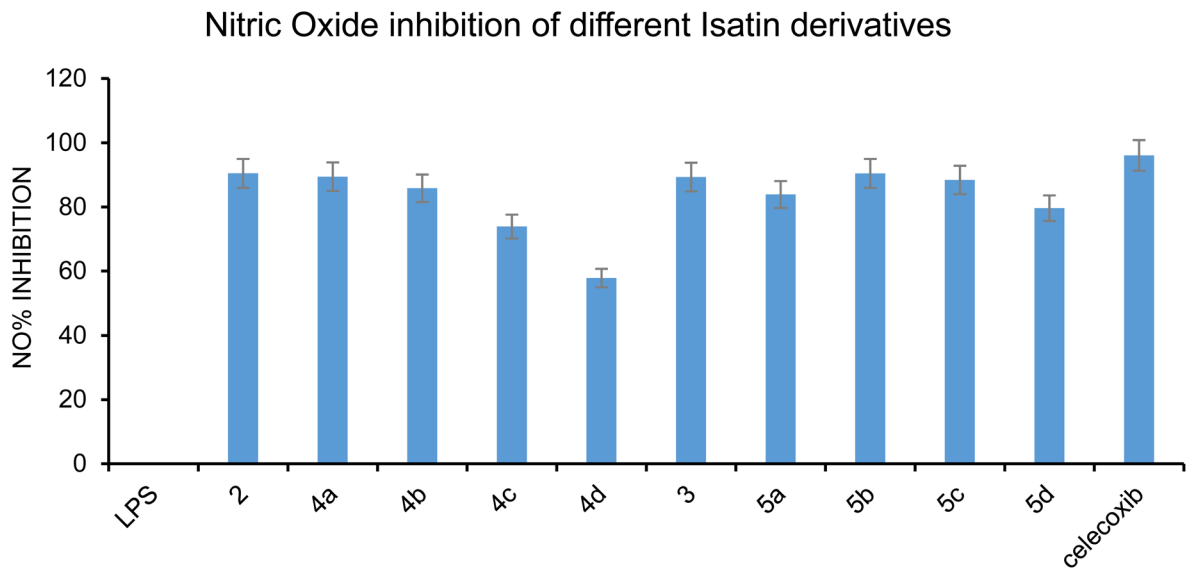

Fig. 4 Effect of isatin analogues (at a concentration of 100 μg mL^{-1}) on nitric oxide levels in LPS- activated Raw macrophages. Raw cells were preincubated for 1 h with isatin derivatives or vehicle (0.025% DMSO) and positive control drug(celecoxib at 100 μg mL^{-1}), followed by LPS stimulation (1 mg mL^{-1}) and further incubated for 24 h at 37 °C. Results are expressed as mean ± SD of three independent experiments performed in triplicate. LPS: lipopolysaccharide.

confirms their potency and supports their potential as promising anti-inflammatory agents.

The observed biological activity may be attributed to the structural features of the isatin scaffold, including its ability to participate in hydrogen bonding and π–π interactions with key amino acid residues in inflammatory target proteins. Additionally, the presence of electron-donating or electron-withdrawing substituents likely influences the compounds' lipophilicity, cellular permeability, and binding affinity, thereby modulating their inhibitory efficacy. These findings provide valuable insights into the structure–activity relationship (SAR) of the synthesized derivatives.

Overall, the significant suppression of NO production underscores the therapeutic potential of these isatin analogs as anti-inflammatory agents. Fig. 3 illustrates the cytotoxicity profile of the tested compounds as evaluated by the MTT assay. The results demonstrate that treatment with the synthesized isatin derivatives did not adversely affect the viability of RAW 264.7 macrophage cells across the tested concentrations. The majority of the compounds maintained high cell viability, indicating minimal cytotoxic effects. This observation confirms that the cells remained metabolically active. The absence of significant cytotoxicity indicates that the observed biological activities of the tested compounds are not attributed to nonspecific cell death. Based on the MTT assay results, it can be concluded that the anti-inflammatory effects are independent of cytotoxic mechanisms. This finding underscores the therapeutic potential of the synthesized compounds, as ideal anti-inflammatory agents should suppress inflammatory mediators without compromising normal cell viability. Therefore, the compounds exhibit a favorable safety profile, supporting their suitability for further pharmacological investigations.

Numerous studies have established that nitric oxide (NO), a short-lived and highly reactive free radical, plays a pivotal role as a signaling molecule in the inflammatory process.[35] The inhibition of NO generation represents a key therapeutic strategy for the development of novel anti-inflammatory agents.

Collectively, the high cell viability observed in the MTT assay validates the reliability of subsequent nitric oxide inhibition studies. The findings confirm that the reduction in NO levels induced by the tested compounds is due to their genuine anti-inflammatory activity rather than cytotoxic effects, thereby highlighting their promise as safe and effective candidates for further *in vitro* and *in vivo* investigations.[35]

Effect of isatin derivatives on TNF-α and interleukin-6. Upon stimulation by external factors, macrophages release cytokines at high levels.

Increased cytokines levels, such as TNF-α and IL-6, lead to dysregulation in the body's immune system, inducing an excessive response that initiates multiple inflammatory conditions.[53] Hence, we investigated the effect of isatin analogues on the different cytokines levels to reveal their role in the inflammatory pathway involving TNF-α and IL-6.

Our results, displayed in Fig. 5a and b, indicated that the LPS-treated cells showed significantly high levels of TNF-α and IL-6 compared to control untreated cells. On the other hand, incubation of cells with isatin analogues resulted in a decline in the levels of both inflammatory mediators. Most compounds displayed significant inhibition of TNF release upon LPS stimulation. However, in the case of IL-6, compounds (**4b**, **5b**, and **4a**) markedly reduced IL-6 release as compared to LPS-treated cells.

Effect of isatin analogues on cyclooxygenase enzyme-II. It was reported that high levels of cyclooxygenase enzyme is an indicative of a persistent inflammatory condition.[54] For further

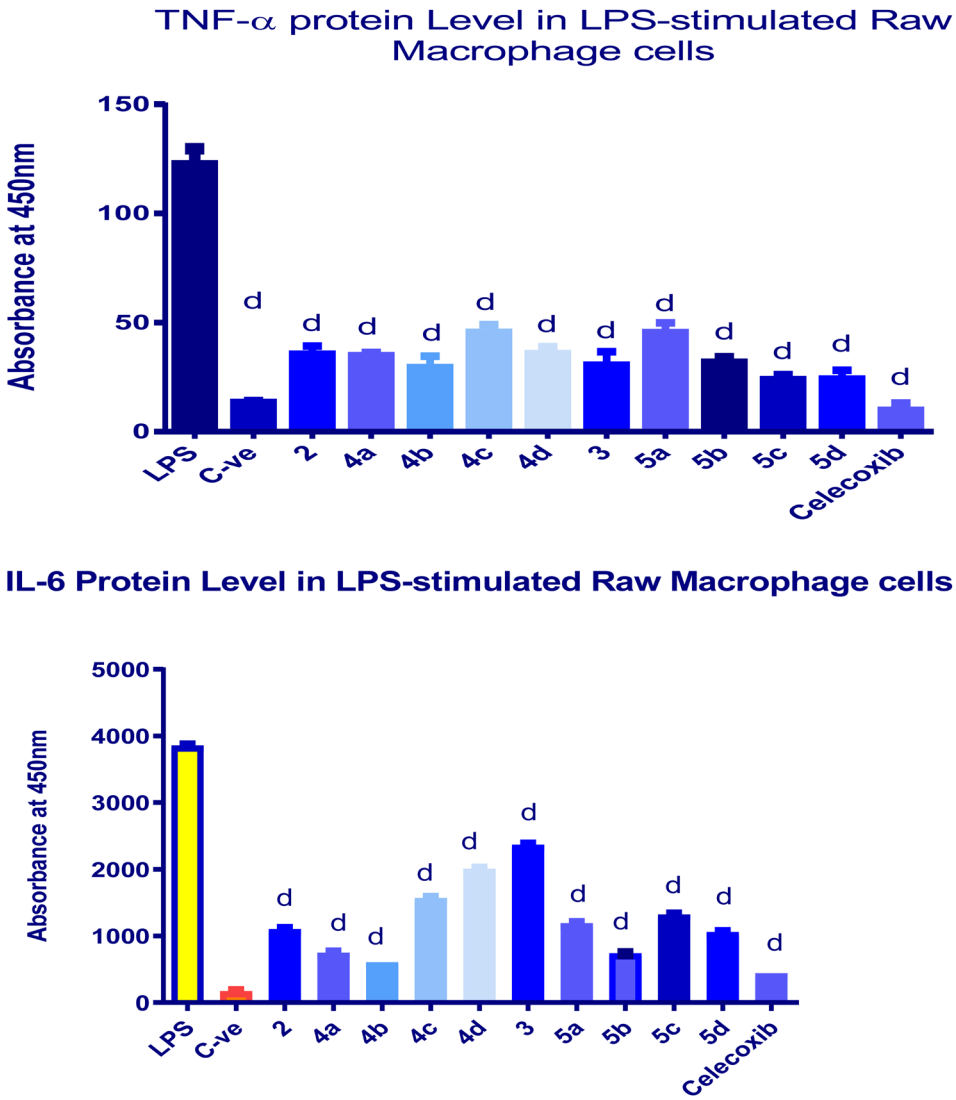

Fig. 5 Effect of isatin derivatives on TNF-α (a) and IL-6 (b) release induced by LPS in RAW 264.7 macrophages. Cells were treated with different compounds for 1 h before LPS treatment. Celecoxib was used as a positive control drug, C−ve: control, negative control, untreated cells. Data are expressed as mean ± SD ($n = 3$). Statistical analysis using GraphPad Prism-one-way (multiple comparison test); $a = p < 0.05$, $b = p < 0.01$, $c = p < 0.001$ and $d = p < 0.0001$ to the LPS-treated cells. ns: means no significant difference. Absorbance was measured at 450 nm.

elucidation of the anti-inflammatory potential of isatin analogues, the level of cyclooxygenase enzyme-II(COX-2) was measured quantitatively by sandwich ELISA. The isatin analogues were incubated with LPS-treated RAW264.7 macrophage cells, followed by estimation of COX-2 levels. As illustrated in Fig. 6, it was observed that the isatin analogues (at the IC_{50} dose) resulted in a reduction of COX-2 levels as compared to LPS-treated cells. Several studies have reported similar results regarding synthetic derivatives of natural products that suppressed COX-2 expression in LPS-induced RAW 264.7 macrophages.[54,55]

Discussion

The activation and differentiation of raw macrophages to dendritic cells required the presence of lipopolysaccharide. Once activated it initiates a cascade of inflammatory mediators.[56] This involves the release of proinflammatory cytokines like tumor necrosis factor-alpha and interleukins (1, 2 and 6).[57] In our present study, it was found that isatin analogues managed to suppress the increase in proinflammatory cytokines in response to LPS activation. It was reported that an activated immune system resulted in excessive production of reactive oxygen species (ROS), disturbing the antioxidant balance and inducing DNA, protein, and lipid damage.[58] The isatin analogues reduced reactive oxygen and nitrogen species accumulation produced by LPS stimulation of macrophages mediated by nitric oxide.[59] The high levels of NO exaggerate the release of more proinflammatory cytokines; concomitantly, these cytokines promote the release of more NO, showing a positive feedback loop that exacerbates the inflammatory process.[60] So, inhibiting nitric oxide release may hinder the

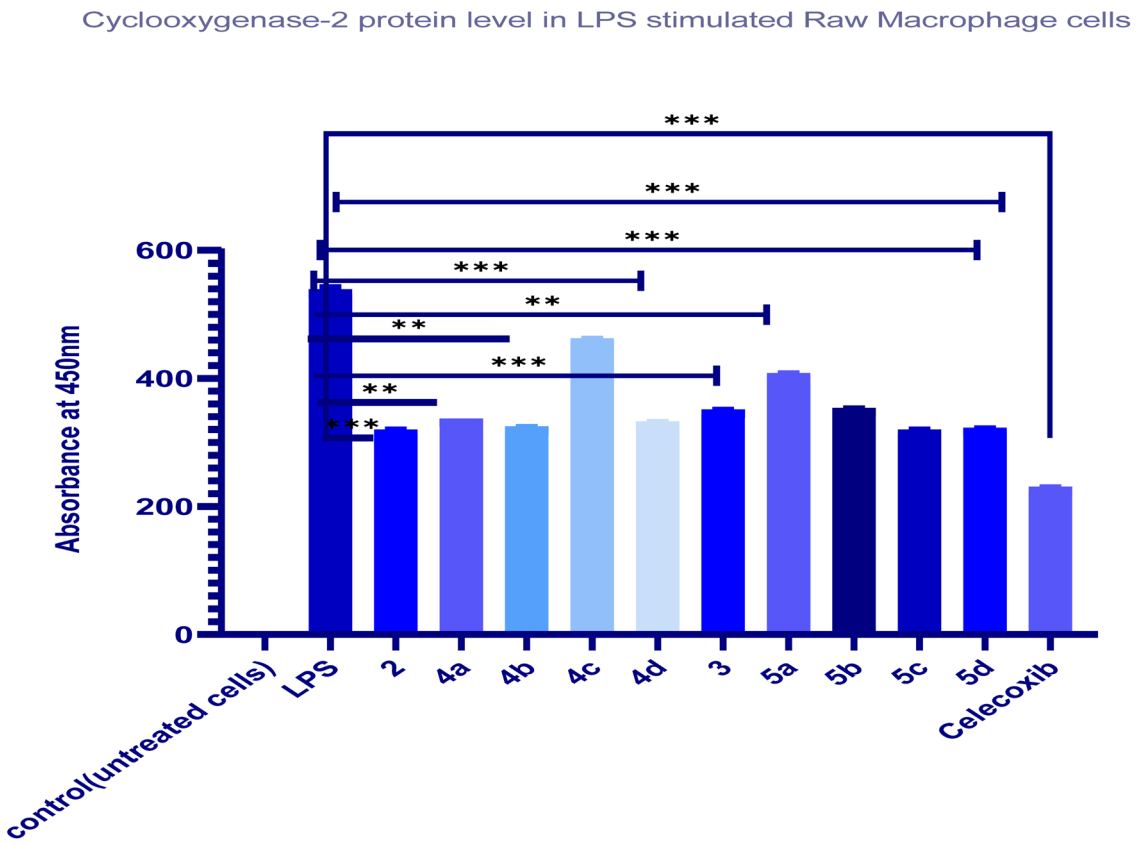

Fig. 6 Effect of isatin analogues on cyclooxygenase enzyme-II levels in LPS in RAW 264.7 macrophages. Cells were treated with different analogues for 1 h before LPS treatment. Following 24 h of incubation, level of Cox-2 were determined in cell supernatant using quantitative Sandwich ELISA technique. Celecoxib was used as a positive control drug. Data are expressed as Mean ± SD ($n = 3$). Statistical analysis using Graph pad prism-one-way (multiple comparison test); * = $p < 0.05$, ** = $p < 0.01$, *** = $p < 0.001$ and **** = $p < 0.0001$ compared to the LPS-treated cells. ns: means no significant difference. LPS: lipopolysaccharide.

inflammatory process. Our results indicated that isatin analogues reduced NO, TNF-α, and IL-6 (Fig. 5a and 4b). It could be concluded that the anti-inflammatory potential of isatin analogues is mediated through NO inhibition.

The overexpression of cyclooxygenase-2 is linked to many chronic inflammatory conditions, including asthma, arthritis, and cancer.[61] The current work indicated that isatin analogues play a role in inhibiting the release of COX-2 and consequent mediators; hence, it may have a potential therapeutic effect in the treatment of various inflammatory conditions.

Structure–activity relationship (SAR) for anti-inflammatory activity

To our knowledge, there aren't many studies that examine the structure–activity correlation (SAR) of isatin and demonstrate its anti-inflammatory capabilities. Regarding the structure–activity relationship (SAR), as illustrated in Fig. 7, a consistent correlation was found between the electrical properties of the substituent aromatic (Ar) groups and the anti-inflammatory effects on tumor necrosis factor-alpha (TNF-α) and interleukin-6 (IL-6).

- The higher anti-inflammatory activity of hydroxyl-substituted derivatives compared with nitro, methoxy, and unsubstituted isatin analogues can be attributed to their enhanced ability to inhibit pro-inflammatory cytokines such as TNF-α and IL-6.[62]
- The hydroxyl (–OH) group acts as both a hydrogen bond donor and acceptor, facilitating strong intermolecular interactions with amino acid residues in biological targets involved in inflammatory signaling pathways. These interactions enhance binding affinity and stabilize ligand-receptor complexes, resulting in a more potent inhibition of cytokine production.[62]

Furthermore, the electron-donating resonance (+M) effect of the hydroxyl group increases electron density within the aromatic system, improving molecular reactivity and biological activity.[63]

- In addition, phenolic hydroxyl groups exhibit significant antioxidant properties by scavenging reactive oxygen species (ROS), which play a crucial role in triggering inflammatory responses and stimulating TNF-α and IL-6 expression.[64] This antioxidant behavior contributes to the downregulation of pro-inflammatory mediators.
- In contrast, the nitro group (–NO_2), a strong electron-withdrawing substituent, reduces electron density and may weaken interactions with biological targets, consequently reducing anti-inflammatory efficacy.[65]

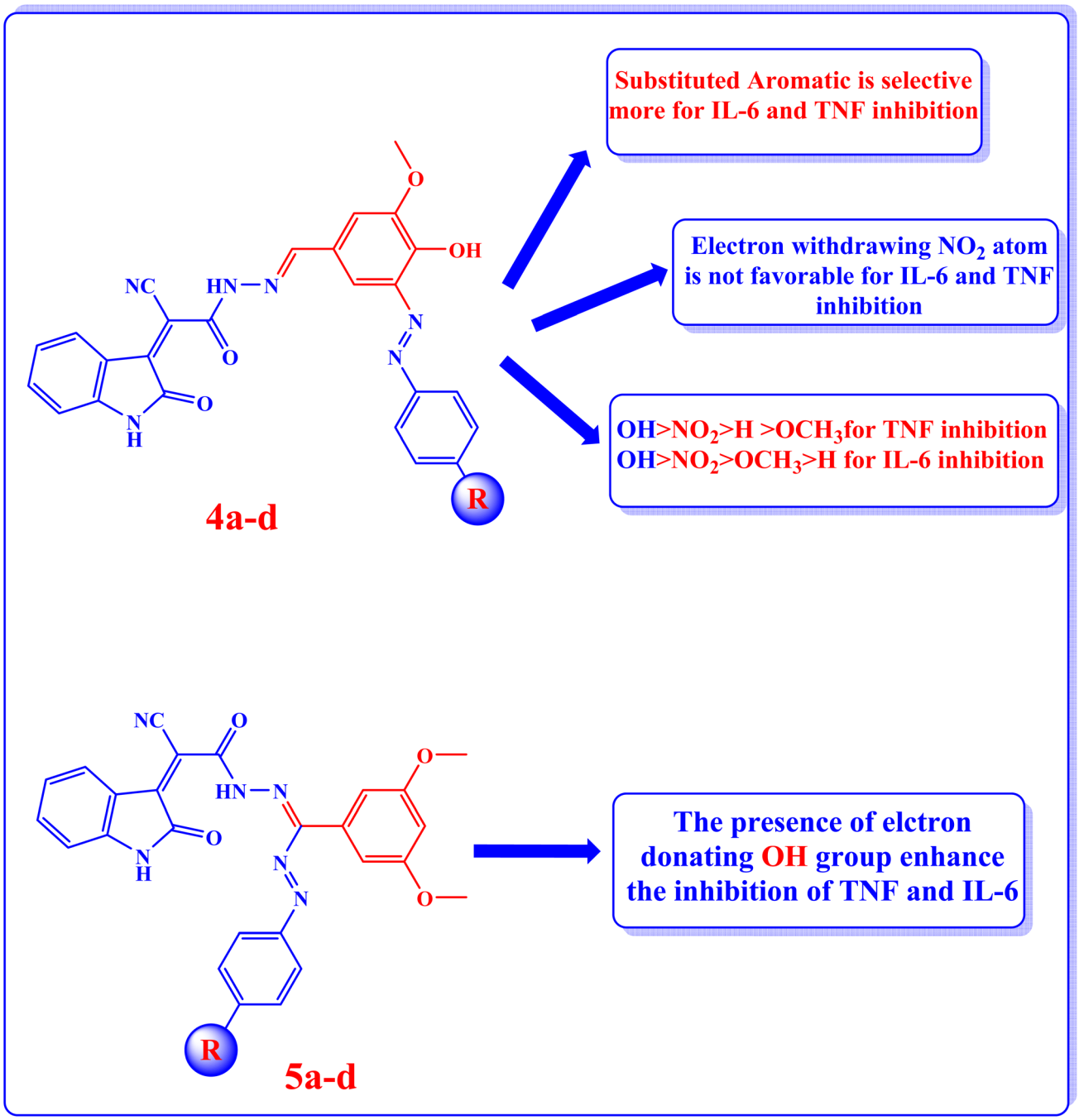

Fig. 7 SAR activity of isatin compounds **4a–d** and **5a–d**.

• The methoxy group ($-OCH_3$), although electron-donating, primarily acts as a hydrogen bond acceptor and introduces steric hindrance due to its methyl moiety, resulting in comparatively lower activity than the hydroxyl group.[65,66]

• Meanwhile, the unsubstituted hydrogen lacks both electronic and hydrogen-bonding contributions, leading to the weakest inhibitory effect.[65]

• From the above discussion, we can conclude that the presence of one or more electron-donating OH groups may enhance the anti-inflammatory activity.

Computational details

Quantum chemical calculations

Molecular modeling procedures and quantum chemistry approaches can specify a wide range of molecule features, including substituents, molecular fragments, reactivity, shape, and binding sites. The relationship between structural factors and isatin dyes' activity was investigated using quantum chemical calculations. The computational study employed the density DFT technique to molecular structures optimization of

the isatin analogs utilizing the Gaussian 09 computer program's implementation of Beck's three-parameter exchange functional (B3LYP) with a 6-311G++ (d, p) basis set. Fig. S7 and S8 display the ideal chemical structure with the lowest energy, as determined by calculations of the substances under investigation.

The results show that compounds **4b** and **5b**, which bear a hydroxyl substituent (electron-donating group) in the aryl aldehyde moiety of the isatin azo dyes, exhibit enhanced biological activity compared to compounds **4a** and **5a** containing a nitro group (electron-withdrawing substituent), Table S2. This behavior is supported by their higher HOMO energies (−5.9871 and −5.8812 eV, respectively, Table S1), indicating an increased ability to donate electrons and interact more effectively with the target protein. In addition, global reactivity descriptors provide further insight into structure–activity relationships. Compounds **4b** and **5b** exhibit the highest softness values (0.8232 and 0.8506 eV, respectively), Table S2, corresponding to smaller HOMO–LUMO energy gaps and greater chemical reactivity.[67,68] This increased softness facilitates charge transfer interactions, which may enhance both enzyme binding and, potentially, color strength due to improved electronic delocalization. Overall, the computational results are in good agreement with the experimental data, demonstrating that electron-

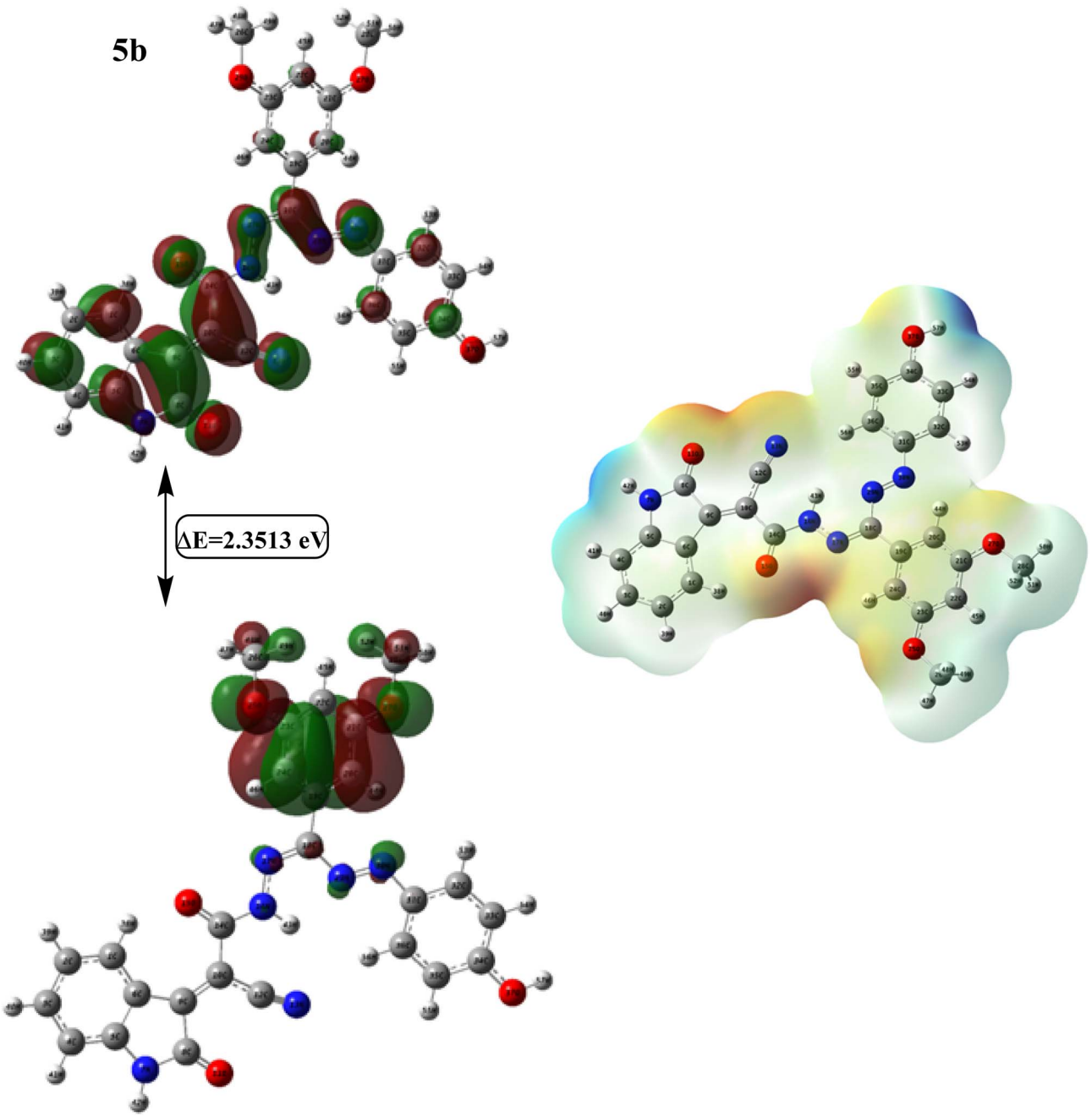

Fig. 8 The HOMO, LUMO, and ESP of the most active compound, **5b**.

donating substituents enhance reactivity, electronic properties, and biological activity of the studied azo dyes.

The frontier molecular orbitals (FMOs)

The highest energy of paired electrons (E_{HOMO}) and the lowest energy of unpaired electrons (E_{LUMO}) can be used to assess the stimulation parameters and the electron's carrying capability.[69–71] They play a crucial role in the molecule's chemical stability.[72] The HOMO is largely an electron donor, whereas the LUMO is primarily an electron acceptor.[73] The molecules' chemical stability and reactivity are determined by the difference between HOMO and LUMO. The B3LYP/6-311G++(d, p) level was used to predict the HOMO–LUMO orbitals, their distributions, and energy levels, as shown in Fig. S26 for every synthesized isatin molecule. The HOMO of isatin dyes **4a–d** mainly disperses charges throughout the vanillin group, which can interact with the biological target as a nucleophile (donor of hydrogen bonds). Their LUMO is delocalized at the isatin moiety, except for compound **4a**, where it distributes charges extended to the nitrophenyl moiety with the vanillin moiety. It interacts with the biological target (hydrogen bond acceptor) by acting as an electrophile. The HOMO of isatin azodyes **5a–d** are localized over the dimethoxy phenyl moiety, and the LUMO are delocalized over the isatin moiety, except for compound **5a**, whose LUMO extends charge to the nitrophenyl moiety with the isatin moiety, Fig. S27.

Molecular electrostatic potential

The molecular electrostatic potential, or MEP, is a three-dimensional representation of molecular charge patterns. Molecular electrostatic potential can be used to connect its dipole moment, electronegativity, residual charges, and chemical reactivity properties.[74] A molecular electrostatic analyzer can be used to examine phenomena such as solvent effects, hydrogen bonding interactions, electrophilic and nucleophilic sites, and other related properties.[75–77] The zones of positive, negative, and neutral potential are expressed by various hues. The red and yellow sections indicate the regions with high electron density, which are associated with electrophilic reactivity.[78] Blue denotes low electron density and nucleophilic reactivity, while white denotes a region with positive electrostatic potential. Conversely, areas of zero potential are represented by green colors.[79] For isatin molecules, to reduce the reactive zone (attacks by electrophile and nucleophile sites), the electrostatic potential of the molecule is computed. The positive, negative, and neutral potential zones are depicted by distinct colors. Electrophilic reactivity is associated with the yellow and red zones, which represent areas of high electron density. White denotes a zone of positive electrostatic potential, whereas a zone of low electron density and nucleophilic reactivity is shown by the color blue. Conversely, green indicates regions with no promise. These areas with different electrostatic potentials can aid in predicting the chemical activity of the molecule and provide valuable insights into various intermolecular interactions. Fig. S28 and S29 display the MEP graphs for the generated compounds, **2,4a–d** and **3,5a–d**, respectively. The molecular electrostatic potential (MEP) maps reveal higher electron density around the oxygen atoms, highlighting favorable sites for electrophilic interactions, which may contribute to improved binding and biological performance. Furthermore, the hydrogen atoms are situated in regions of positive potential, marking them as likely centers for nucleophilic interaction due to their electron-deficient nature.

The electronic distribution of frontier orbitals (HOMO & LUMO) and ESP of the most active compound is shown in Fig. 8.

Vibrational spectra

The correlation between the estimated and observed wavenumbers of the isatin molecules utilizing the DFT/B3LYP/6-311G++ (d, p) method, Tables S2 and S3. Examples of the computed and observed infrared spectral data are shown in Fig. S30 and S31. The correct wavenumber assigned to a given vibration is determined by comparing the estimated and actual wavenumbers. The difference in wave number measurements between the estimated and actual numbers can be explained by comparing the phase of solids data with theoretical estimates for the gaseous phase.[80] For isatin analogs **4a–d**, the broadband (3320–3419 cm^{-1}) shown in the experiment is caused by the symmetric stretching vibrations of the N–H group, whereas the computed band is about 3490 cm^{-1}. Also, studying the isatin azodyes absorbed in (1454–1460) cm^{-1} (experimental) and at (1448–1465) cm^{-1} (calculated) may depend on the stretching vibration of the N=N azo group. Furthermore, the measured variation ν(C=O), ν(C=N), and ν(C≡N) were observed at about 1720 cm^{-1}, (1657–1668) cm^{-1}, and (2102–2158 cm^{-1}), respectively, and the calculated vibrations are 1708, 1646, and 2231 cm^{-1}, respectively, Table S3. On the other hand, for isatin azodyes **5a–d**, the stretching vibration of the crucial N=N group is observed at 1436–1458 cm^{-1}(calculated), and 1454–1463 cm^{-1}(observed). The nitrile group appears at about 2235 cm^{-1} (theoretical) and at about 2250 (experimental). Furthermore, the carbonyl and imine groups are observed at about 1707 and 1450 cm^{-1} (calculated), respectively, and at about 1720 and 1590 cm^{-1} (experimentally), respectively, Table S4. As shown by the linear correlation (R) value of 0.998 in Fig. S32 and S33, the computed and experimental results demonstrate a high level of accuracy.

Molecular docking study of compound 5b within the TNF (tumor necrosis factor) binding site

HVEM is a TNF (tumor necrosis factor) receptor that supports a variety of immunological processes involving many cell types. It interacts with immunoglobulin (Ig) superfamily members BTLA and CD160, as well as a TNF ligand called LIGHT. The variety of interactions between HVEM and HVEM binding partners has made it difficult to evaluate the functional impact of HVEM binding to certain ligands in various contexts. In order to examine the molecular foundations of different roles, we obtained crystal structures that display the distinct HVEM surfaces that engage with LIGHT or BTLA/CD160, including the human being HVEM-LIGHT-CD160 ternary complex, where HVEM interacts with both binding partners concurrently. Based

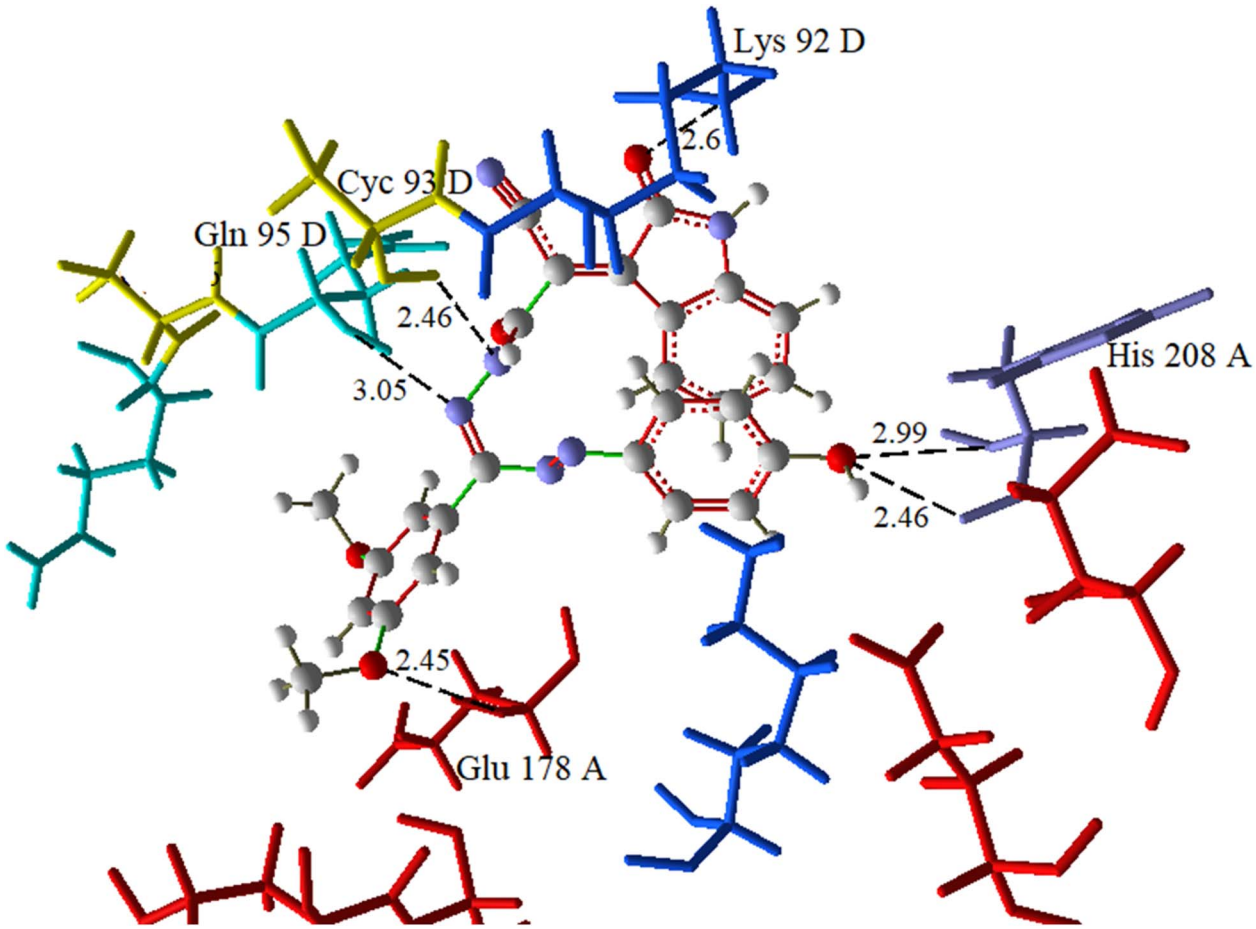

Fig. 9 Compound **5b**'s binding interactions within TNF's active site (PDB ID: 4RSU). The interacting amino acid residues are depicted as sticks, colored according to their chains, while the ligand is displayed as ball and stick. Hydrogen bond interactions are shown by dashed lines.

on these structures, we created mouse HVEM mutants that precisely identified the TNF or Ig ligands *in vitro*. In knock-in mice expressing these mutants, all the proteins in the HVEM network are produced; however, they show distinct roles for Ig ligands in reducing hepatic inflammation and LIGHT in eliminating intestinal microorganisms.[81]

Molegro Virtual Docker (MVD)[82] was implemented for molecular docking examinations in order to assess the docking technique utilizing the crystal structure of the TNF complex. The optimized molecular structure for **5b** molecule acquired from DFT/B3LYP/6-311+G(d, p) estimations were utilized as input file for conformational search using systematic search route. The lowest energy conformer was utilized for the docking simulation. Our studies began with the examination of the known structure acquired Protein Data Bank (PDB ID: 4RSU with resolution of 2.3 Å). The co-crystallized NAG: 2-acetamido-2-deoxy-beta-D-glucopyranose used to try out the validation of the docking method. With a grid box radius of 8 Å, the docking grid was centered at coordinates $X = 23.62$, $Y = -16.33$, and $Z = 96.14$, guaranteeing that the full TNF active site was covered. Standard precision settings were used in the docking process to replicate the simulated ligand binding pose. Excellent concordance between the anticipated and observed poses was demonstrated by the root-mean-square deviation (RMSD) of 2.0 Å obtained from superimposing the docked and crystal ligand conformations, Fig. S34. This demonstrates the validity and suitability of the chosen docking procedure and grid parameters for ensuing virtual screening and structure-based TNF medication discovery.

Key residues Gln95 (chain D), Leu94 (chain D), and Glu178 (chain A) create additional stabilizing bonds of hydrogen with the natural ligand, Fig. S34. These interactions contribute to the overall binding capacity and specificity by anchoring the ligand in the TNF binding cleft. The recognized physiological characteristics necessary for TNF inhibition are in line with these suggested relationships.

A strong and sustained binding affinity between the ligand and the TNF protein was shown by the docking simulation of compound **5b**, which produced a binding score of -155.035 kcal mol^{-1}, a rerank score of -107.22 kcal mol^{-1}, and a hydrogen bond interaction energy of -8.847 kcal mol^{-1}. Multiple hydrogen bonds, hydrophobic contacts, and favorable docking parameters indicate that compound **5b** successfully stabilizes within the TNF active site, confirming its possible inhibitory function, which is consistent with the experimental findings.

Compound **5b**'s binding contacts within the TNF's active site are seen in Fig. 9, emphasizing the network of hydrophobic and hydrogen bond interactions that support the compound's stability

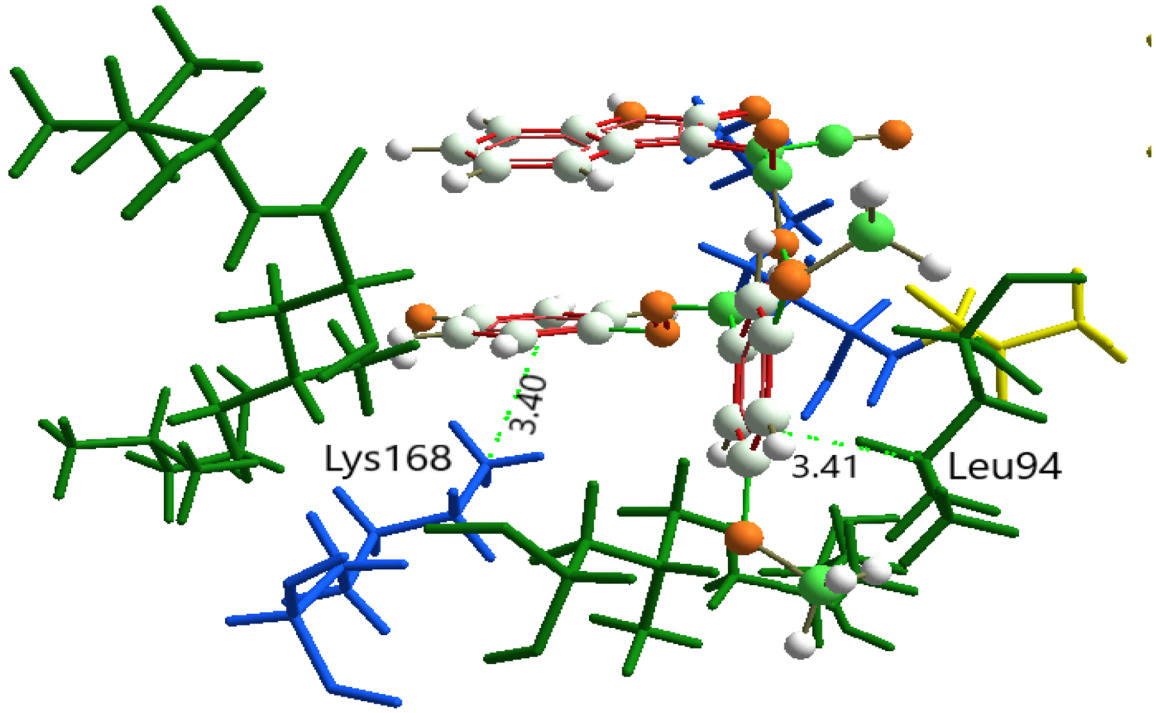

Fig. 10 The hydrophobic interactions of compound **5b** inside the TNF binding site (PDB ID: 4RSU). Key amino acid residues of the TNF receptor surround the ligand, which is shown in a ball-and-stick image. Through van der Waals interactions, hydrophobic residues like Leu94 (green) create a nonpolar pocket that stabilizes the ligand. Lys168 (blue).

and affinity. Critical amino acid residues of the TNF binding cleft surround the ligand, which is depicted in stick form (gray carbon framework) and colored stick format based on residue type and chain. A detailed inspection of the interaction map reveals that compound **5b** forms multiple hydrogen bonds with key residues within chains A and D of TNF. Specifically, hydrogen bonding interactions are observed with Glu178(A) (2.45 Å), Lys92(D) (2.6 Å), Gln95(D) (3.05 Å), and Cyc93(D) (2.46 Å), along with a stabilizing interaction with two hydrogen bonds with His208(A) at 2.99 and 2.46 Å. Strong and directed hydrogen bonding, which is known to

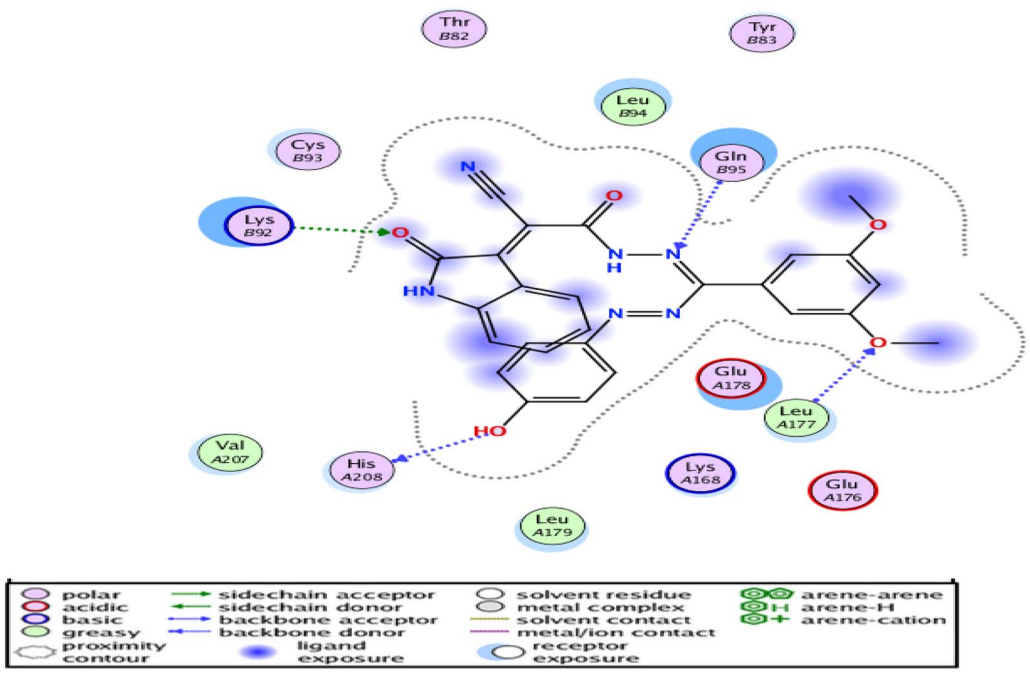

Fig. 11 Compound **5b**'s two-dimensional interaction diagram inside TNF's binding pocket (PDB ID: 4RSU). Hydrogen bonds are depicted as green (donor) and blue (acceptor) dashed lines in the black stick image of the ligand.

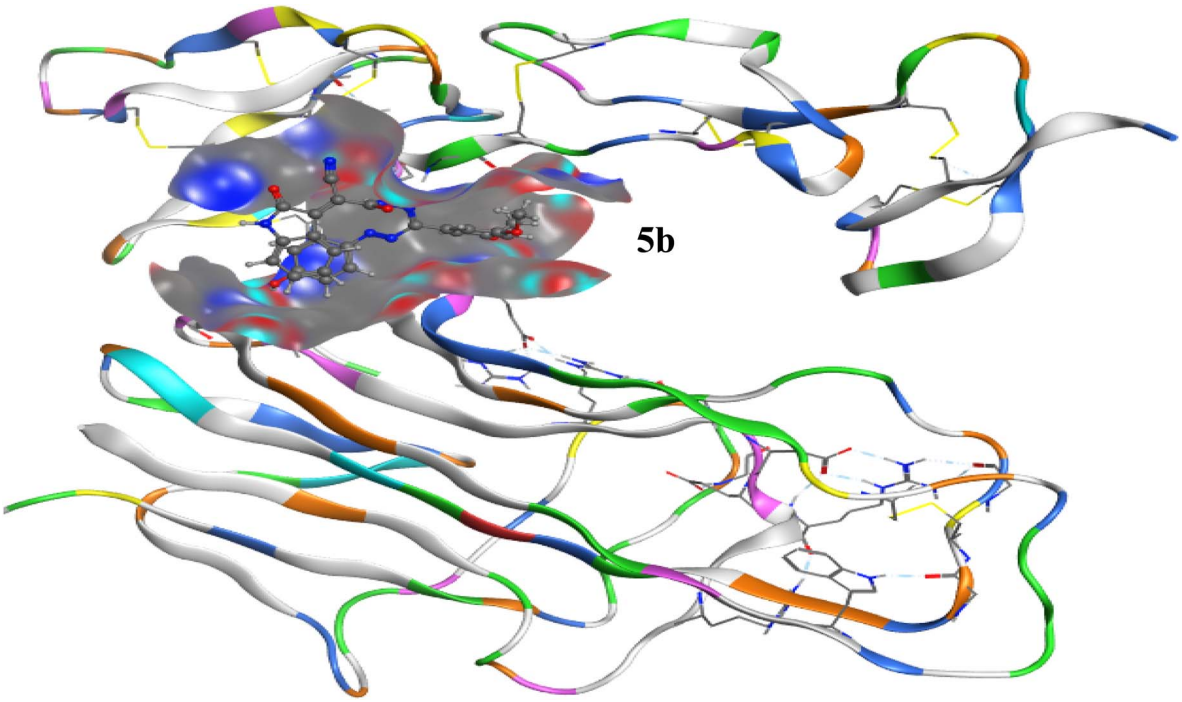

Fig. 12 Compound **5b**'s three-dimensional surface inside the TNF binding pocket. The ligand is depicted with its molecular electrostatic surface, and the TNF protein is displayed as a ribbon diagram colored according to secondary structure (α-helices, β-sheets, and loops).

improve ligand binding stability inside the TNF binding pocket, is suggested by these short bond lengths (range from 2.4–3.05 Å). Additionally, hydrophobic interactions are formed with Leu94(D) (3.41 Å) and Lys168(A) (3.40 Å), Fig. 10, which together add to the hydrophobic enclosure surrounding the aromatic rings of the ligand. The molecule is further anchored in the receptor cavity by this environment, which promotes π–π stacking and van der Waals stability. The important residues that stabilize compound **5b**'s binding to the TNF receptor are clearly shown in the 2D interaction map, Fig. 11. The spatial orientation of the ligand within the binding pocket of the receptor is depicted in the 3D structural visualization of compound **5b** complexed with TNF, Fig. 12.

Conclusion

Isatin azodyes 2-cyano-*N*′-(4-hydroxy-3-methoxy) (*E*)-(Aryl) diazinyl) benzylidene)-2-((*Z*)-2-oxoindolin-3-ylidene) acetohydrazide (**4a–d**), and (*E*)-5-(2-cyano-2-((*Z*)-2-oxoindolin-3-ylidene) acetyl)-3-(3,5-dimethoxyphenyl)-1-(Aryl) formazan (**5a–d**) were created, and several spectroscopic techniques were used to clarify their structures. The azo compounds with electron-donating OH groups, **4b** and **5b**, demonstrated the strongest anti-inflammatory effects of all the azo dyes. Moreover, the most potent designed derivative, **5b**, interacts with TNF's amino acid residues through hydrophobic and hydrogen bonding interactions, according to a study utilizing molecular docking of the receptor. These computations can be applied to the preselection of fresh, strong candidates, which is currently primarily based on empirical data. Key hydrogen bonding and non-covalent interactions with residues such as Lys92, Gln95, Glu178, His208, Leu94, and Lys168 support the inhibitory potency of compound **5b**. Furthermore, the agreement between the docked pose and the co-crystallized ligand validates the reliability of the docking protocol. The estimated FT-IR data were also computed to determine the compounds' distinctive vibration frequencies, which demonstrated a strong connection with the experimental data. Therefore, our research identifies compound **5b** as a promising targeted inhibitory candidate against COX-2, TNF-α, and IL-6, with significant potential as an anti-inflammatory agent. However, further investigations including gene expression analyses, protein-level studies, and *in vivo* evaluations are necessary to validate their mechanisms of action and confirm their safety and efficacy.

Additionally, the synthesis of new hydroxyl-substituted azo dyes is recommended to investigate and optimize their anti-inflammatory properties.

Author contributions

All authors contributed equally to the writing, review, and methodology.

Conflicts of interest

The authors have no relevant financial or non-financial interests to disclose.

Data availability

The data supporting this article have been included as part of the supplementary information (SI). Supplementary information is available. See DOI: https://doi.org/10.1039/d6ra01392a.

References

1 R. Sahilu, R. Eswaramoorthy, E. Mulugeta and A. Dekebo, *J. Mol. Struct.*, 2022, **1265**, 133279.
2 T. Tahir, *Molecules*, 2021, **26**, 4872.
3 B. N. Ravi, K. J, M. N. M, V. Kumar and S. Kandgal, *J. Mol. Struct.*, 2020, **1204**, 127493.
4 S. Benkhaya, S. M'rabet and A. El Harfi, *Heliyon*, 2020, **6**, e03271.
5 A. Y. Alzahrani, H. F. Rizk, Z. K. Hamza and S. Elkhabiry, *Fibers Polym.*, 2024, **25**, 3819–3828.
6 S. S. Ragab, A. M. K. Sweed, Z. K. Hamza, E. Shaban and A. A. El-Sayed, *Fibers Polym.*, 2022, **23**, 2114–2122.
7 A. Laurent, Recherches sur l'indigo, *Ann. Chim. Phys.*, 1841, **3**, 371–383.
8 O. L. Erdmann, Untersuchungen über den Indigo, *J. Prakt. Chem*, 1840, **19**, 321–362.
9 S. Ke, L. Shi and Z. Yang, *Bioorg. Med. Chem. Lett.*, 2015, **25**, 4628–4631.
10 V. S. Pawar, *Med. Chem. Res.*, 2011, **20**, 370–380.
11 S. Y. Abbas, *Monatshefte für Chemie – Chem. Mon.*, 2013, **144**, 1725–1733.
12 C. Liang, *Eur. J. Med. Chem.*, 2014, **74**, 742–750.
13 A. Jarrahpour, J. Sheikh, I. E. Mounsi, H. Juneja and T. B. Hadda, *Med. Chem. Res.*, 2013, **22**, 1203–1211.
14 R. Raj, *Chem. Biol. Drug Des.*, 2014, **83**, 622–629.
15 V. Eggadi, U. Kulandaivelu, S. B. B. Sheshagiri and V. J. Rao Jupalli, *Pharm. Chem.*, 2016, **3**, 4–9.
16 E. Rajanarendar, S. Ramakrishna, K. Govardhan Reddy, D. Nagaraju and Y. N. Reddy, *Bioorg. Med. Chem. Lett.*, 2013, **23**, 3954–3958.
17 A. El-Faham, *J. Chem.*, 2015, **2015**, 716987.
18 P. Mondal, S. Jana, A. Balaji, R. Ramakrishna and L. K. J. Kanthal, *Young Pharm.*, 2012, **4**, 38–41.
19 S. Firke, *Lett. Drug Des. Discov.*, 2021, **18**, 1146–1164.
20 P. Meshram, *J. Mol. Struct.*, 2025, **1322**, 140508.
21 T. Aysha, *Color. Technol.*, 2015, **131**, 333–341.
22 M. El-Sedik, S. Abd Elmegied, T. Aysha and S. Mahmoud, *Egypt. J. Chem.*, 2019, **12**, 1810.
23 K. N. Houk and F. Liu, *Acc. Chem. Res.*, 2017, **50**, 539–543.
24 Y. D. Scherson, S. J. Aboud, J. Wilcox and B. J. Cantwell, *J. Phys. Chem. C*, 2011, **115**, 11036–11044.
25 F. M. Atlam and H. A. Hekal, *J. Iran. Chem. Soc.*, 2023, **20**, 1949–1973.
26 H. A. Hekal, M. M. Salem and H. A. A. El Salam, *BMC Chem.*, 2024, **18**, 174.
27 M. M. Kabanda, *Int. J. Electrochem. Sci.*, 2012, **7**, 5035–5056.
28 M. Ma, Y. Sun and G. Sun, *Dye. Pigment.*, 2003, **58**, 27–35.
29 R. Abd El-Aal, *Dye. Pigment.*, 2004, **60**, 205–214.
30 Z. A. Elshahid, A. Salama and S. A. Gouhar, *Adv. Tradit. Med.*, 2024, **24**, 265–283.
31 M. Hamed, H. Mohamed, Z. El Shahed, M. Abdel-Aziz and E. El-Wakil, *Egypt. J. Chem.*, 2024, **67**(9), 1–12.
32 M. M. Eid, *J. Inorg. Organomet. Polym. Mater.*, 2022, **32**, 931–940.
33 G. E. Ahmed, Z. A. Elshahid, E. R. El-Sawy, M. S. Abdel-Aziz and A. Abdel-Aziem, *Sci. Rep.*, 2024, **14**, 9106.
34 M. D. Al-Ameedee, *Al-Mustansiriyah j. pharm. sci.*, 2025, **25**(4), 581–591.
35 A. Granados, R. Pleixats and A. Vallribera, *Molecules*, 2021, **18**, 3008.
36 M. Liu, A. Guinart, A. Granados, C. Gimbert-Suriñach, E. Fernández, R. Pleixats and A. Vallribera, *ACS Appl. Mater. Interfaces*, 2024, **27**, 14595–14604.
37 M. R. Mahmoud, A. K. El-Ziaty, F. S. M. A. El-Azm, M. F. Ismail and S. A. Shiba, *J. Chem. Res.*, 2013, **37**, 80–85.
38 R. S. Berns and D. M. Reiman, *Canadian Society for Color*, 2002, **27**, 360–373.
39 J. Hu, P. Skrabal and H. Zollinger, *Dyes Pigm.*, 1987, **8**, 189–209.
40 P. Savarino, *Dyes Pigm.*, 1989, **11**, 163–172.
41 H. A. Abd El Salam, M. S. Abdel-Aziz, E. R. El-Sawy and E. Shaban, *Fibers Polym.*, 2023, **24**, 2751–2760.
42 K. Mahmoud, *Toxicon*, 2024, **244**, 107752.
43 T. Mosmann, *J. Immunol. Methods*, 1983, **65**, 55–63.
44 O. S. Oni, K. A. Bello and M. A. Shibdawa, *IOSR J. Appl. Chem.*, 2019, **12**(3–1), 36–46.
45 S. Aslam, B. Ali, S. Murtaza and N. Shafiq, *Mater. Adv.*, 2025, **6**, 6991–7015.
46 A. Z. Omar, A. M. Khamis and E. A. Hamed, *Sci. Rep.*, 2023, **13**, 21554.
47 T. Azetsu and N. Suetake, *Designs*, 2021, **5**, 32.
48 (*a*) S. D. Kim, M. J. Kim, B. S. Lee and K. S. Lee, *Fibers Polym.*, 2004, **5**, 39–43; (*b*) A. Z. Omar, A. S. Mohamed, E. A. Hamed, S. M. El-Badry and M. A. El-atawy, *J. Mol. Liq.*, 2024, **407**, 125216.
49 A. M. Al-Etaibi, H. S. Alnassar and M. A. El-Apasery, *Molecules*, 2016, **21**(7), 855.
50 M. Elapasery, F. A. Yassin, M. H. Abd El-Azim, M. E. Abdellatif and H. Mashaly, *Egypt. J. Chem.*, 2020, **63**(9), 3209–3216.
51 M. O. Saleh, M. A. El-Apasery, A. M. Hussein, A. B. A. El-Adasy and M. M. Kamel, *Egypt. J. Chem.*, 2021, **12**(1), 64–68.
52 J. O. Otutu and E. Osabohien, *Orient. J. Chem.*, 2009, **25**(4), 863.
53 M. Tajdari, *Iran. J. Pharm. Res.*, 2024, **23**(1), e151312.
54 K. Koopklang, *Molecules*, 2024, **29**, 603.
55 Z.-Z. Liu, J.-C. Ma, P. Deng, F.-C. Ren and N. Li, *Molecules*, 2023, **28**, 2685.
56 J. Hwang, J. Ma, J. Park, H. Jung and Y. Park, *Int. J. Mol. Med.*, 2018, **2018**, 3937.
57 M. J. Manzari Tavakoli, *Inflamm. Res.*, 2020, **13**, 487–495.
58 Z. Wang, *Carbohydr. Polym.*, 2021, **251**, 117129.
59 D. Malayil, N. C. House, D. Puthenparambil, J. T. Job and A. Narayanankutty, *Drug Chem. Toxicol.*, 2022, **45**, 1716–1722.
60 L. Zhang, J. Chen, H. Liao, C. Li and M. Chen, *J. Funct. Foods*, 2020, **75**, 104217.
61 M. Yang, *J. Ethnopharmacol.*, 2020, **261**, 113105.
62 A. N. Kumar, S. R. Das, J. K. Kumar, K. V. N. S. Srinivas and S. D. Tetali, *RSC Adv.*, 2025, **15**(3), 2023–2033.

63 M. S. Rana, N. M. A. Rayhan, M. S. H. Emon, M. T. Islam, K. Rathry, M. M. Hasan and M. A. Asraf, *RSC advances*, 2024, **14**(45), 33094–33123.
64 H. Ueda, C. Yamazaki and M. YamazakiI, *Biosci. Biotechnol. Biochem.*, 2004, **68**, 119–125.
65 D. Dimitrova, S. Manolov, I. Ivanov, D. Bojilov, L. Kasamova and P. Nedialkov, *Molbank*, 2024, **2024**(1), M1775.
66 X. Wang, H. Liu, M. Sun, F. Gao, X. Feng, M. Xu and D. Sun, *Chem. Commun.*, 2025, **61**(57), 10538–10541.
67 P. W. Ayers and R. G. Parr, *J. Am. Chem. Soc.*, 2000, **122**, 2010–2018.
68 R. G. Parr, R. A. Donnelly, M. Levy and W. E. Palke, *J. Chem. Phys.*, 1978, **68**, 3801–3807.
69 R. H. Waghchaure and V. A. Adole, *J. Mol. Struct.*, 2024, **1296**, 136724.
70 S. Miertuš, E. Scrocco and J. Tomasi, *Chem. Phys.*, 1981, **55**, 117–129.
71 S. Anand and A. Muthusamy, *J. Mol. Struct.*, 2019, **1177**, 78–89.
72 V. A. Adole, A. Kumar, N. Misra, R. A. Shinde and B. S. Jagdale, *Polycycl. Aromat. Compd.*, 2024, **44**, 5397–5411.
73 R. A. Shinde, V. A. Adole, R. D. Amrutkar, S. R. Tambe and B. S. Jagdale, *Polycycl. Aromat. Compd.*, 2024, **44**, 5530–5552.
74 R. A. Shinde, V. A. Adole and B. S. Jagdale, *J. Mol. Struct.*, 2024, **1300**, 137096.
75 H. S. Deshmukh, *J. Mol. Struct.*, 2024, **1305**, 137745.
76 S. Moro, M. Bacilieri, C. Ferrari and G. Spalluto, *Curr. Drug Discov. Technol.*, 2005, **2**, 13–21.
77 Y. Li, *Molecules*, 2013, **18**, 877–893.
78 F. Weinhold and C. R. Landis, *Chem. Educ. Res. Pr.*, 2001, **2**, 91–104.
79 K. B. Gangurde, V. A. Adole and D. S. Ghotekar, *Results Chem.*, 2023, **6**, 101093.
80 N. Subramanian, N. Sundaraganesan and J. Jayabharathi, *Spectrochim. Acta Part A Mol. Biomol. Spectrosc.*, 2010, **76**, 259–269.
81 W. Liu, *J. Exp. Med.*, 2021, **218**(12), e20211112.
82 G. Bitencourt-Ferreira and W. F. de Azevedo Jr., *Methods Mol. Biol.*, 2019, **2053**, 149–167.